EUROPEAN ORGANISATION FOR NUCLEAR RESEARCH (CERN)

October 3, 2021

Report from the NA61/SHINE experiment at the CERN SPS

The NA61/SHINE Collaboration

This document reports on the status and plans of the NA61/SHINE experiment at the CERN SPS as of October 2021. The document refers to the proposal SPSC-P-330.

CERN-SPSC-2021-027 / SPSC-SR-298
03/10/2021

Contents

The NA61/SHINE Collaboration

A. Acharya[12], H. Adhikary[12], K.K. Allison[28], N. Amin[5], E.V. Andronov[24], T. Antićić[3], M. Baszczyk[16], S. Bhosale[13], A. Blondel[4], M. Bogomilov[2], Y. Bondar[12], A. Brandin[23], A. Bravar[26], W. Bryliński[20], J. Brzychczyk[15], M. Buryakov[22], O. Busygina[21], H. Cherif[6], M. Ćirković[25], M. Csanad [7,8], J. Cybowska[20], T. Czopowicz[12,20], A. Damyanova[26], N. Davis[13], M. Deveaux[6], A. Dmitriev [22], W. Dominik[18], P. Dorosz[16], J. Dumarchez[4], R. Engel[5], G.A. Feofilov[24], L. Fields[27], Z. Fodor[7,19], M. Friend[9], A. Garibov[1], M. Gaździcki[6,12], O. Golosov[23], V. Golovatyuk [22], M. Golubeva[21], K. Grebieszkow[20], F. Guber[21], A. Haesler[26], S.N. Igolkin[24], S. Ilieva[2], A. Ivashkin[21], S.R. Johnson[28], K. Kadija[3], N. Kargin[23], E. Kashirin[23], M. Kiełbowicz[13], V.A. Kireyeu[22], V. Klochkov[6], R. Kolesnikov[22], D. Kolev[2], A. Korzenev[26], J. Koshio[10], V.N. Kovalenko[24], S. Kowalski[17], M. Koziel[6], B. Kozłowski[20], A. Krasnoperov[22], W. Kucewicz[16], M. Kuich[18], A. Kurepin[21], A. László[7], T.V. Lazareva[24], M. Lewicki[19], K. Łojek[15], G. Lykasov[22], V.V. Lyubushkin[22], M. Maćkowiak-Pawłowska[20], Z. Majka[15], B. Maksiak[14], A.I. Malakhov[22], A. Marcinek[13], A.D. Marino[28], K. Marton[7], H.-J. Mathes[5], T. Matulewicz[18], V. Matveev[22], G.L. Melkumov[22], A.O. Merzlaya[15], B. Messerly[29], Ł. Mik[16], S. Morozov[21,23], Y. Nagai [8], T. Nakadaira[9], M. Naskręt[19], V. Ozvenchuk[13], O. Panova[12], V. Paolone[29], O. Petukhov[21], I. Pidhurskyi[6], R. Płaneta[15], P. Podlaski[18], B.A. Popov[22,4], B. Porfy[7,8], M. Posiadała-Zezula[18], D.S. Prokhorova[24], D. Pszczel[14], S. Puławski[17], J. Puzović[25], M. Ravonel[26], R. Renfordt[6], D. Röhrich[11], E. Rondio[14], M. Roth[5], B.T. Rumberger[28], M. Rumyantsev[22], A. Rustamov[1,6], M. Rybczynski[12], A. Rybicki[13], S. Sadhu[12], A. Sadovsky[21], K. Sakashita[9], K. Schmidt[17], I. Selyuzhenkov[23], A.Yu. Seryakov[24], P. Seyboth[12], M. Słodkowski[20], P. Staszel[15], G. Stefanek[12], J. Stepaniak[14], M. Strikhanov[23], H. Ströbele[6], T. Šuša[3], A. Taranenko[23], A. Tefelska[20], D. Tefelski[20], V. Tereshchenko[22], A. Toia[6], R. Tsenov[2], L. Turko[19], M. Unger[5], D. Uzhva[24], F.F. Valiev[24], D. Veberič[5], V.V. Vechernin[24], A. Wickremasinghe[29,27], K. Wójcik[17], O. Wyszyński[12], A. Zaitsev[22], E.D. Zimmerman[28], and R. Zwaska[27]

[1] National Nuclear Research Center, Baku, Azerbaijan
[2] Faculty of Physics, University of Sofia, Sofia, Bulgaria
[3] Ruđer Bošković Institute, Zagreb, Croatia
[4] LPNHE, University of Paris VI and VII, Paris, France
[5] Karlsruhe Institute of Technology, Karlsruhe, Germany
[6] University of Frankfurt, Frankfurt, Germany
[7] Wigner Research Centre for Physics of the Hungarian Academy of Sciences, Budapest, Hungary
[8] Eötvös Loránd University, Budapest, Hungary
[9] Institute for Particle and Nuclear Studies, Tsukuba, Japan
[10] Okayama University, Japan
[11] University of Bergen, Bergen, Norway
[12] Jan Kochanowski University in Kielce, Poland
[13] Institute of Nuclear Physics, Polish Academy of Sciences, Cracow, Poland
[14] National Centre for Nuclear Research, Warsaw, Poland
[15] Jagiellonian University, Cracow, Poland
[16] AGH - University of Science and Technology, Cracow, Poland
[17] University of Silesia, Katowice, Poland
[18] University of Warsaw, Warsaw, Poland
[19] University of Wrocław, Wrocław, Poland
[20] Warsaw University of Technology, Warsaw, Poland
[21] Institute for Nuclear Research, Moscow, Russia
[22] Joint Institute for Nuclear Research, Dubna, Russia
[23] National Research Nuclear University (Moscow Engineering Physics Institute), Moscow, Russia
[24] St. Petersburg State University, St. Petersburg, Russia
[25] University of Belgrade, Belgrade, Serbia
[26] University of Geneva, Geneva, Switzerland
[27] Fermilab, Batavia, USA
[28] University of Colorado, Boulder, USA
[29] University of Pittsburgh, Pittsburgh, USA

The NA61/SHINE Limited Members

N. Antoniou[1], P. Banasiak[6], S. Bordoni[7], N. Charitonidis[7], P. Christakoglou[1], G. Christodoulou[7], A. De Roeck[7], F. Diakonos[1], P. von Doetinchem[2], S.J. Dolan[7], D. Gawliński[6], M. Grzelak[6], S. Jędrzejewski[6], A. Kapoyannis[1], J. Kempa[6], U. Kose[7], D.R. Kowcun[6], M.O. Kuttan[4], O. Linnyk[4], W.C. Louis[3], B. Meller[6], C. Mussolini[7], A.D. Panagiotou[1], T. Pawlak[6], J. Pawlowski[4], D. Piotrowski[6], W. Rauch[5], S. Schramm[4], A. Shukla[2], J. Steinheimer-Froschauer[4], H. Stoecker[4], M. Vassiliou[1], C.F. Vilela[7], J. Wiktorowicz[6], and K. Zhou[4]

[1] University of Athens, Athens, Greece
[2] University of Hawaii at Manoa, USA
[3] Los Alamos National Laboratory, USA
[4] Frankfurt Institute for Advanced Studies, Frankfurt, Germany
[5] Fachhochschule Frankfurt, Frankfurt, Germany
[6] Warsaw University of Technology Plock Campus, Poland
[7] CERN, Geneva, Switzerland

1 Introduction

This annual report presents the status and plans of the NA61/SHINE experiment [1] at the CERN SPS. The report refers to the period October 2020 - October 2021.

The document is organized as follows. New results are presented in Section 2. Status of the software and calibration upgrades is summarized in Section 3. An overview of the hardware upgrade is given in Section 4. The beam request for 2022 and plans for data taking in 2023-2024 are presented in Section 5. The summary in Section 6 closes the paper.

An addendum to the NA61/SHINE Proposal entitled *Letter of Intent for a Low-Energy Beamline at the SPS H2* is submitted to the SPS Committee in parallel to this report.

2 New results

2.1 New results for strong interactions physics

The NA61/SHINE strong interactions program is based on beam momentum scans (13A – 150A/158A GeV/c) with light and intermediate-mass nuclei (from p+p to Xe+La). The main physics goals include searching for the second-order critical end-point in the temperature versus baryo-chemical potential phase diagram and studying the properties of deconfinement's onset. In recent years, the program has been extended by Pb+Pb collisions where the open charm production and collective effects are studied.

This section summarizes new preliminary and recently published physics results from the program on physics of strong interactions. The results on spectra and yields as well as on fluctuations and correlations are presented. They are labeled according to the NA61/SHINE physics goals, i.e., the study of the onsets of deconfinement (OD) [2] and fireball (OF) [3], the search for the critical point (CP) and others (O).

2.1.1 (OD, OF) Published results on π^- production in central Be+Be collisions at 19A–150A GeV/c

The final results on π^- spectra and yields in the 5% most central Be+Be collisions at 19A–150A GeV/c were already discussed in the previous Status Report, and they were published in Ref. [4].

2.1.2 (OD, OF) Published results on π^+, π^-, K^+, K^-, p, and $\bar{p}$ in central Be+Be collisions at 19A–150A GeV/c

The final results on π^+, π^-, K^+, K^-, p, and $\bar{p}$ spectra and yields in the 20% most central Be+Be collisions at 19A–150A GeV/c were published in Ref. [5]. The example plots from the paper are discussed below. Spectra presented in the publication include: i) $K^\pm$ based on *tof*-dE / dx method at 30A–150A GeV/c, ii) $K^\pm$, $\pi^\pm$ and protons based on dE / dx method at 19A–150A GeV/c, iii) anti-protons at 40A–150A GeV/c based on dE / dx method.

The new NA61/SHINE measurements of the inverse slope parameter T at mid-rapidity in the 20% most central Be+Be collisions are shown versus collision energy for K^+ and K^- in Fig. 1. The Be+Be results are similar to published results from inelastic p+p interactions [6].

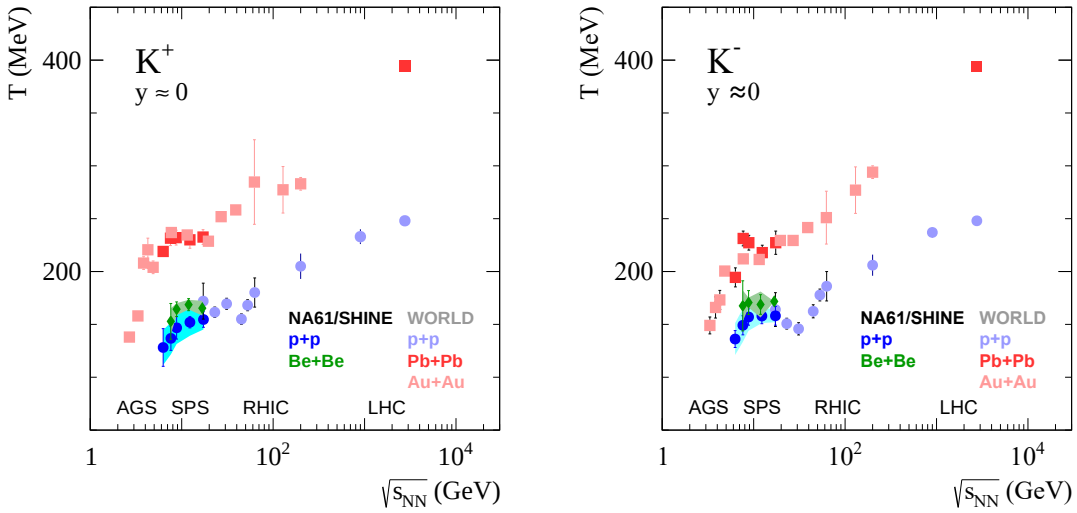

Figure 1: The energy dependence of the inverse slope parameter of p_T spectra at mid-rapidity of positively (*left*) and negatively (*right*) charged K mesons for central Be+Be, Pb+Pb, and Au+Au collisions as well as inelastic p+p interactions. Both statistical (vertical bars) and systematic (shaded bands) uncertainties are shown.

This indicates that not much expansion flow is created in the small, like Be+Be, collision systems at the SPS energies. Although there appears to be a similar step feature, the values of T are much smaller than those from collisions of heavy nuclei.

The results for the energy dependence of the K^+/π^+ ratio from the 20% most central Be+Be collisions are shown in Fig. 2 together with measurements in inelastic p+p, central Pb+Pb, and central Au+Au collisions. The results from Be+Be collisions do not yet deviate from those in p+p reactions and are about a factor two lower for the total yield ratio than the values found in central Pb+Pb and Au+Au collisions. In particular, no horn structure is observed for the small collision systems. Note that in Be+Be (and p+p) collisions, the $K^\pm$ and π^- yields were measured by NA61/SHINE over all of phase space. This was not possible for the π^+ yield, which had to be derived from the π^- yield using an isospin correction. Be+Be collisions, however, are isospin symmetric, and therefore the mean multiplicities of π^+ and π^- have to be the same. The π^- yields for the 20% most central Be+Be collisions were calculated by scaling the π^- multiplicity published in Ref. [4] by the ratio of mean numbers of nucleons $\langle W \rangle$ for the 20% and the 5% most central Be+Be collisions.

2.1.3 (OD, OF) Published results on π^- production in central Ar+Sc collisions at 13A–150A GeV/c

The final results on π^- spectra and yields in the 5% most central Ar+Sc collisions at 13A–150A GeV/c were published in Ref. [7]. The example plots from the paper are discussed below.

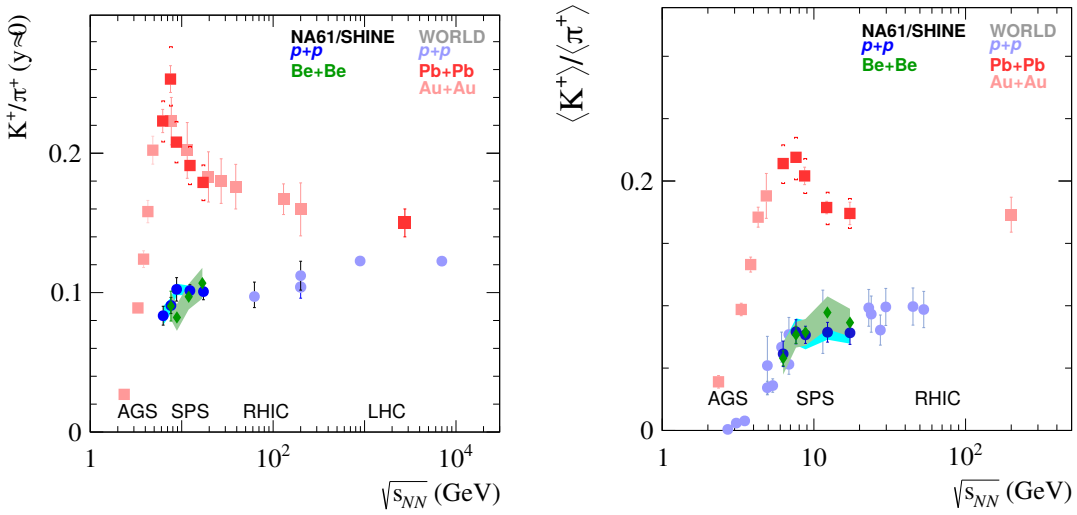

Figure 2: The energy dependence of the K^+/π^+ particle yields ratio at mid-rapidity (*left*) and full acceptance (*right*) for the 20% most central Be+Be, central Pb+Pb, and Au+Au collisions, as well as inelastic *p+p* interactions. Both statistical (vertical bars) and systematic (shaded bands) uncertainties are shown.

The energy dependence of the sound velocities extracted from the data is presented in Fig. 3. The energy range for results from central Ar+Sc, central Be+Be, and inelastic *p+p* interactions is too limited, and the fluctuations in the data too large to allow a significant conclusion about a possible minimum. Data on central Pb+Pb collisions, in combination with results from AGS and RHIC on central Au+Au collisions, cover a much wider energy range. Here the sound velocity exhibits a clear minimum (usually called the softest point) at $\sqrt{s_{NN}} \approx 10$ GeV consistent with the reported onset of deconfinement [8,9].

Fig. 4 shows the *kink* plot, the dependence of the ratio of the mean number of pions produced in a collision to the mean number of wounded nucleons $\langle\pi\rangle/\langle W\rangle$ versus the Fermi energy measure, which is expressed as:

$$F = \left[\frac{(\sqrt{s_{NN}} - 2m_N)^3}{\sqrt{s_{NN}}}\right]^{1/4} \approx \sqrt[4]{s_{NN}}, \tag{1}$$

where $\sqrt{s_{NN}}$ is the collision energy per nucleon pair in the center of mass. Systematic uncertainty connected with the calculation of the number of wounded nucleons $\langle W\rangle$ was not included in the systematic uncertainties plotted in Fig. 4. The uncertainty was of the order of 5%.

Interestingly, $\langle\pi\rangle/\langle W\rangle$ for Ar+Sc reactions equals that for *N+N*[1] reactions at low SPS energies, whereas it is consistent with that for central Pb+Pb reactions at high SPS energies. A suppression of pion yield per wounded nucleon in central Pb+Pb collisions compared to *N+N* reactions is observed at low energies, which is not found for the intermediate size Ar+Sc system. This effect was attributed to pion absorption in the evolving fireball [13,14]. The behavior of Ar+Sc stands in contradiction to Be+Be measurements, which are close to

[1] For *p+p* interactions the figure shows isospin symmetrized values [10] marked as *N+N*.

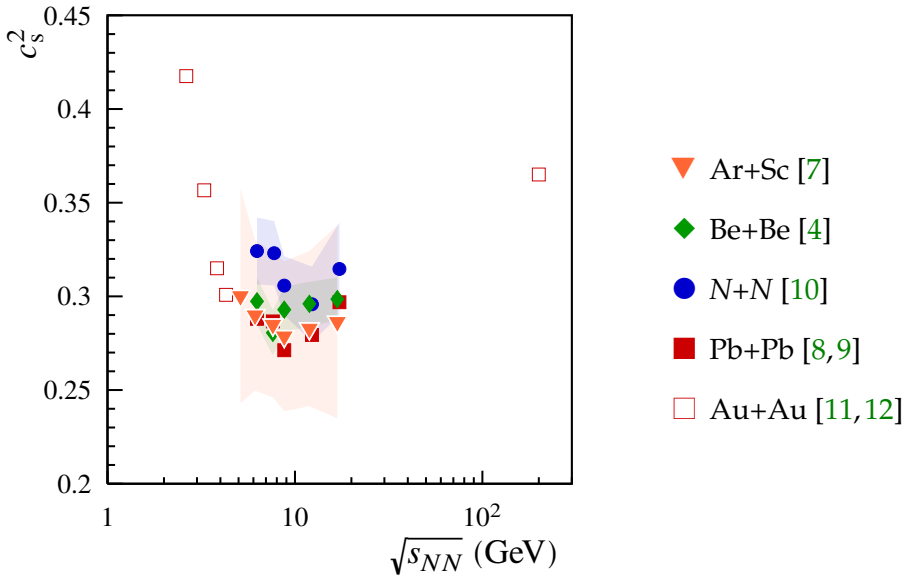

Figure 3: The speed of sound c_s^2 as a function of center-of-mass collision energy (per nucleon pair) as extracted from the data.

the Pb+Pb results except for the top SPS beam energy. The steepening of the slope of the $\langle\pi\rangle/\langle W\rangle$, which is considered a signal of the onset of deconfinement within the SMES [15] model, is not observed in *central* Ar+Sc measurements.

2.1.4 (O) Published results on two-particle correlations in azimuthal angle and pseudorapidity in central Be+Be collisions at 19A–150A GeV/c

The final results on two-particle $\Delta\eta\Delta\phi$ correlations in the 5% most central Be+Be collisions at 19A–150A GeV/c were already discussed in the previous Status Report, and they were published in Ref. [19].

2.1.5 (CP) Published results on multiplicity fluctuations of identified hadrons in inelastic p+p collisions at 31–158 GeV/c

The final results on multiplicity fluctuations of identified hadrons (so-called chemical fluctuations) in inelastic p+p collisions at 31–158 GeV/c were already discussed in the previous Status Report, and they were published in Ref. [20].

2.1.6 (O) Final results on $\Xi(1530)^0$ and $\overline{\Xi}(1530)^0$ production in inelastic p+p collisions at 158 GeV/c

The final results on $\Xi(1530)^0$ and $\overline{\Xi}(1530)^0$ spectra and yields in inelastic p+p collisions at 158 GeV/c were submitted to arXiv [21] and have been just accepted by Eur. Phys. J. C. The example plots from the paper are discussed below.

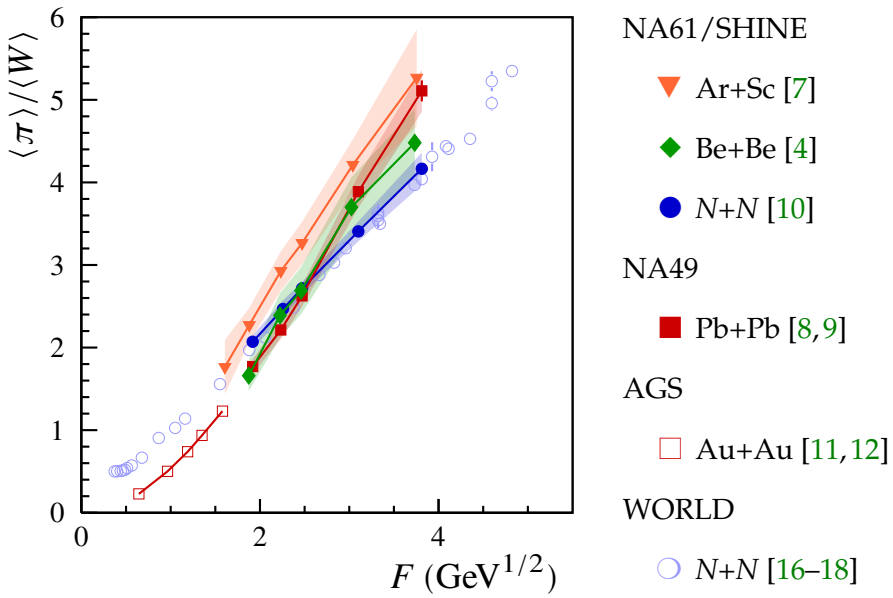

Figure 4: The *kink* plot showing the ratio of the mean pion multiplicity $\langle \pi \rangle$ to the mean number of wounded nucleons $\langle W \rangle$ versus the Fermi energy variable $F \approx \sqrt[4]{s_{NN}}$. Results for inelastic nucleon-nucleon reactions and central nucleus-nucleus collisions are compared.

The NA61/SHINE measurements on double-differential spectra and mean multiplicities of $\Xi(1530)^0$ and $\overline{\Xi}(1530)^0$ resonances produced in inelastic p+p interactions were presented [21]. The results were obtained from a sample of $26{\cdot}10^6$ inelastic p+p events at 158 GeV/c beam momentum ($\sqrt{s_{NN}} = 17.3$ GeV). The measured rapidity (see Fig. 5) and transverse momentum distributions were extrapolated to full phase space, and mean multiplicities of $\Xi(1530)^0$ equal $(6.73 \pm 0.25 \pm 0.67){\times}10^{-4}$ and $\overline{\Xi}(1530)^0$ equal $(2.71 \pm 0.18 \pm 0.18){\times}10^{-4}$ were obtained. The $\overline{\Xi}(1530)^0/\Xi(1530)^0$ yields ratio at mid-rapidity was found to be $0.54 \pm 0.06 \pm 0.07$.

Results were also compared with predictions of the hadron-resonance gas (HRG) model [22] in the canonical (CE) formulation. They are shown in Fig. 6. The equilibrium version of the model (Fig. 6, *left*) strongly disagrees with the data. This disagreement is much reduced by allowing for out-of-equilibrium strangeness production (Fig. 6, *right*). The result indicates strong suppression of strange particle production in inelastic p+p collisions.

2.1.7 (O, OD) Final results on K^0_S production in inelastic p+p collisions at 158 GeV/c

The final results on K^0_S spectra and yield in inelastic p+p collisions at 158 GeV/c were submitted to arXiv [28] and Eur. Phys. J. C. The example plots from the paper are discussed below.

Measurements of double-differential spectra and mean multiplicity of K^0_S meson produced in inelastic p+p interactions at beam momentum of 158 GeV/c were performed. The K^0_S yields in

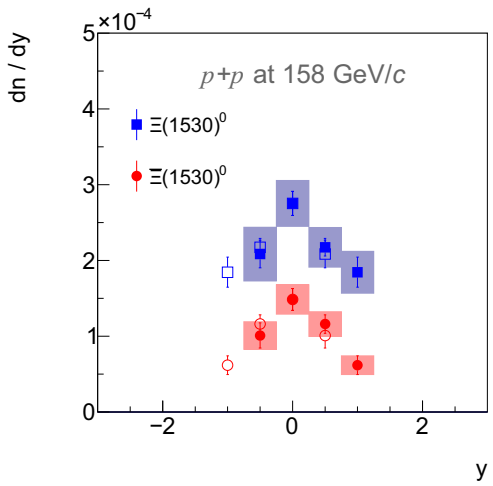

Figure 5: Rapidity spectra of $\Xi(1530)^0$ (full blue squares) and $\overline{\Xi}(1530)^0$ (full red circles) produced in inelastic p+p interactions at 158 GeV/c. Statistical uncertainties are shown by vertical bars, and shaded bands correspond to systematic uncertainties of the measurements. The empty symbols correspond to the values reflected around mid-rapidity.

different rapidity bins were obtained from the corresponding measured transverse momentum distributions. The extrapolation to the high p_T region outside of the acceptance was performed using equation $f(p_T) = A \cdot p_T \cdot \exp(\sqrt{p_T^2 + m_0^2}/T)$, where m_0 is the mass of the K_S^0 and T is the inverse slope parameter. In Fig. 7, the resulting dn/dy spectrum was compared with predictions from microscopic and statistical models EPOS1.99 [29,30], UrQMD 3.4 [31,32], SMASH 2.0 [33], and PHSD [34,35]. The EPOS1.99 model describes the experimental data fairly well while all other models overpredict the K_S^0 yield by 10–20%.

The mean multiplicity of K_S^0 mesons was calculated as the sum of measured points in Fig. 7 and the integral below linear functions through the last two measured points on both sides representative for the unmeasured region (for rapidity $y < -1.75$ and $y > 2.25$). The obtained mean multiplicity of 0.162 ± 0.001 (stat.) $\pm$ 0.015 (sys.) was compared in Fig. 8 with the world data in the energy range from 3 to 32 GeV [36–52]. The measured values are seen to rise linearly with collision energy $\sqrt{s_{NN}}$; the NA61/SHINE result follows the observed trend.

2.1.8 (CP) Preliminary results on proton intermittency in Ar+Sc at 150A GeV/c and Pb+Pb at 30A GeV/c

Results from the intermittency analysis in transverse momentum space in cumulative variables of mid-rapidity protons produced in inelastic Ar+Sc collisions at 150A GeV/c and Pb+Pb collisions at 30A GeV/c have been released as preliminary.

These analyses have examined the behavior of the Second Scaled Factorial Moments of the proton multiplicity distributions with an increasing number of bins in transverse momentum

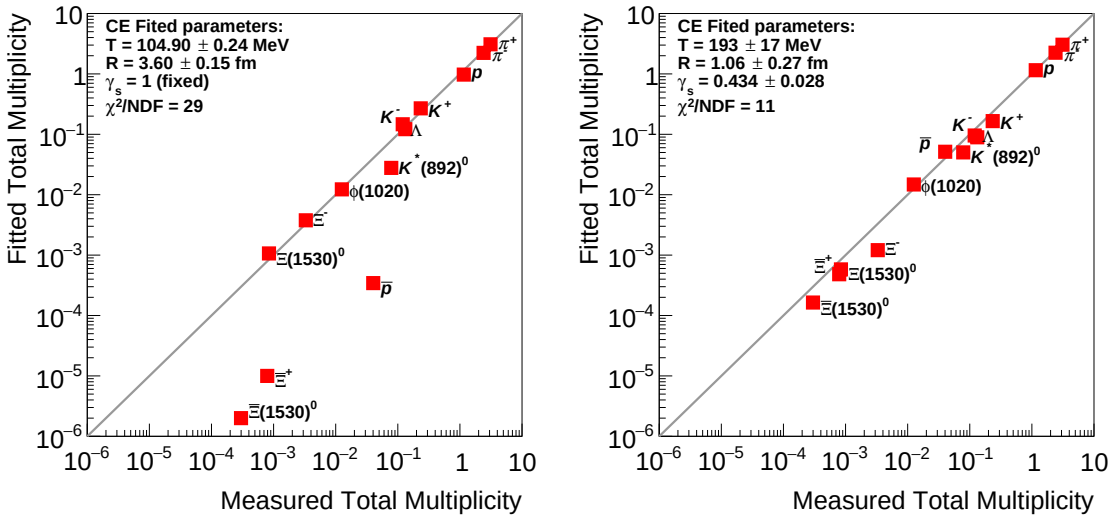

Figure 6: Mean multiplicities of π^+, π^-, K^+, K^-, p, $\overline{p}$, $K^*(892)^0$, Λ, $\phi(1020)$, Ξ^-, $\overline{\Xi}^+$, $\Xi(1530)^0$ and $\overline{\Xi}(1530)^0$ produced in p+p interactions at 158 GeV/c [6, 10, 21, 23–27] measured by NA61/SHINE compared with mean multiplicities obtained from the HRG model based on the Canonical Ensemble with fixed strangeness suppression factor $\gamma_s = 1$ (*left*) and fitted γ_s (*right*). Uncertainties of the measurement are smaller than the symbol size.

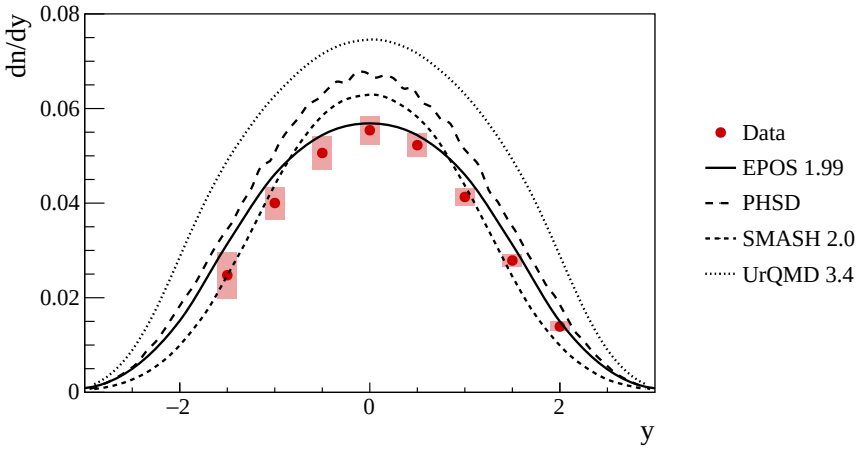

Figure 7: Comparison of the results on the K^0_S rapidity distribution in inelastic p+p collisions at 158 GeV/c with predictions of theoretical models. Colored red circles show the new measurements of NA61/SHINE. The black curves show predictions of models: EPOS1.99 (full), PHSD (long dashed), SMASH 2.0 (short dashed), and UrQMD 3.4 (dotted).

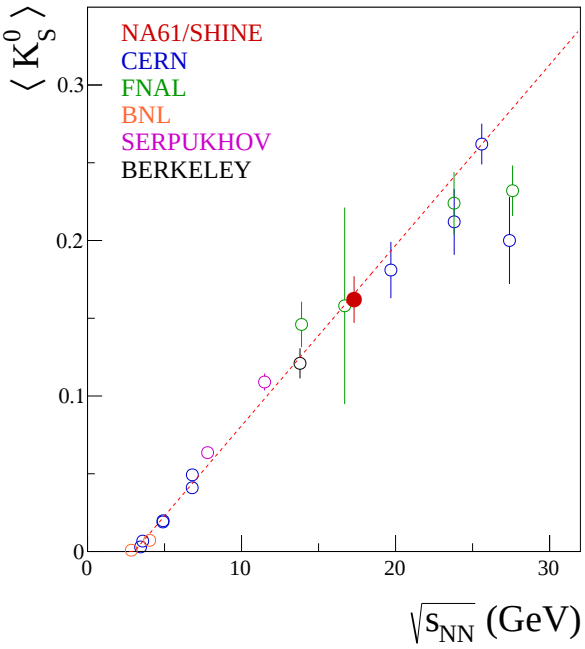

Figure 8: Collision energy dependence of mean multiplicity of K^0_S mesons produced in p+p interactions. The full colored red circle shows the measurement by NA61/SHINE presented with its systematic uncertainty. The results published by other experiments are presented with open circles colored in blue (CERN), green (FNAL), orange (BNL), magenta (SERPUKHOV), and black (BERKELEY). The references for the plotted data points are given in the text.

(decreasing transverse momentum bin sizes), $F_2(M)$. The Scaled Factorial Moment of the order r is defined as:

$$F_r(M) = \frac{\left\langle \frac{1}{M}\sum_{i=1}^{M} n_i(n_i-1)...(n_i-r+1) \right\rangle}{\left\langle \frac{1}{M}\sum_{i=1}^{M} n_i \right\rangle^r}, \tag{2}$$

where n_i denotes the number of particles in i-th bin and $\langle ... \rangle$ averaging over events.

When the system is a simple fractal and $F_r(M)$ follows a power-law dependence:

$$F_r(M) \sim (M)^{\varphi_r}. \tag{3}$$

Additionally, the exponent (intermittency index) φ_r obeys the relation:

$$\varphi_r = (r-1) \cdot d_r, \tag{4}$$

where the anomalous fractal dimension d_r is independent of r.

To eliminate the dependence on the single-particle transverse momentum distribution, its components, p_x and p_y, have been transformed into their cumulative equivalents [53]. This

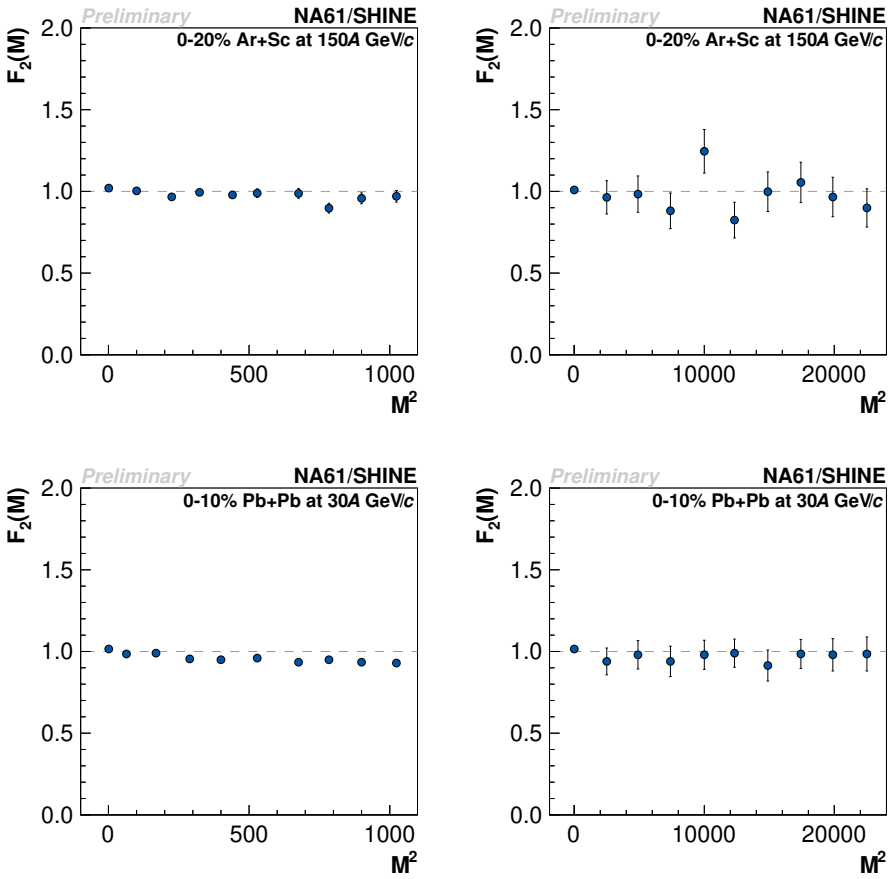

Figure 9: Proton intermittency preliminary results using cumulative variables for 0–20% central Ar+Sc collisions at 150A GeV/c (*top*) and 0–10% central Pb+Pb interactions at 30A GeV/c (*bottom*). Plots were obtained for limited M (1 . . . 32) bins (*left*) and for $M = 1 \ldots 150$ bins (*right*).

transformation was proven to preserve the critical power-law dependence on M. Moreover, the $F_2(M)$ values for different M are independent, as each data point was calculated using a separate sub-sample of available events. This removes possible undesirable correlation but at the cost of limited statistics.

An independent study has shown that the momentum resolution of the detector would distort the critical power law. The effect is not negligible but can be reduced by limiting the range of studied values of M. Thus the released results include both ranges, i.e. up to M=150 and M=32.

The obtained results are presented in Fig. 9. No signal of power-law increase was observed in Ar+Sc at 150A GeV/c and Pb+Pb at 30A GeV/c. These results have been presented in Refs. [54, 55].

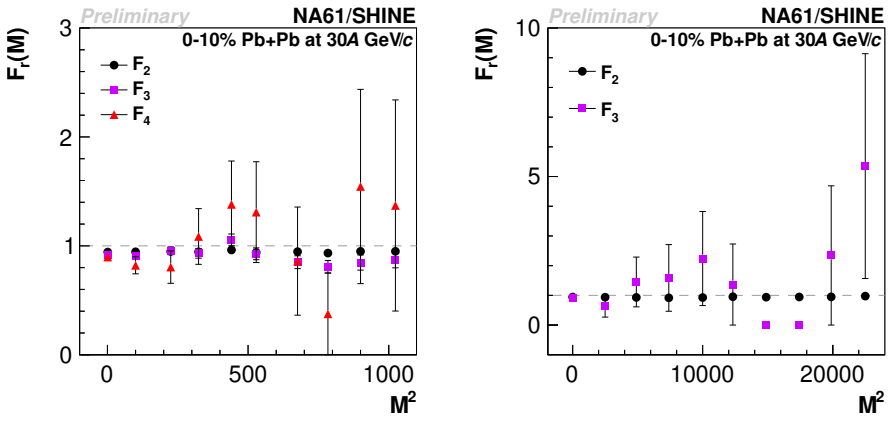

Figure 10: Preliminary results on negatively charged hadrons intermittency using cumulative variables in 0–10% central Pb+Pb interactions at 30A GeV/c. Plots were obtained for limited M (1 . . . 32) bins (*left*) and for $M = 1 \ldots 150$ bins (*right*).

2.1.9 (CP) Preliminary results on the intermittency of negatively charged hadrons in Pb+Pb at 30A GeV/c

Results from the intermittency analysis in transverse momentum space in cumulative variables of mid-rapidity negatively charged hadrons produced in inelastic Pb+Pb collisions at 30A GeV/c have been released as preliminary.

This analysis was similar to proton intermittency – it has studied the behavior of the Scaled Factorial Moments of the negatively charged hadrons multiplicity distributions with an increasing number of bins in transverse momentum. However, the number of produced negatively charged hadrons is sufficient to study up to the fourth moment, i.e., $F_2(M)$, $F_3(M)$ and $F_4(M)$.

The obtained results are presented in Fig. 10. No signal of power-law increase was observed in Pb+Pb at 30A GeV/c. The results from Fig. 10 (*left*) have been presented in Refs. [55,56].

2.1.10 (CP) Preliminary results on rapidity dependence of higher-order moments of multiplicity and net-charge in inelastic p+p collisions at 158 GeV/c

The expected signal of a critical point is a non-monotonic dependence of various fluctuation/correlation measures in system size or energy scan. A specific property of the CP – the increase in the correlation length – makes fluctuations its basic signal. Special interest is devoted to fluctuations of conserved charges (electric, strangeness, or baryon number). To compare fluctuations in systems of different sizes, one should use intensive quantities, i.e. quantities insensitive to the system volume. Such quantities are constructed by the ratio of cumulants κ_i of the measured distribution (up to fourth order), where i is the order of the cumulant, e.g. κ_2/κ_1. Fluctuations depend on phase-space coverage of measurements. By changing it, one is sensitive to different measurement conditions. Preliminary results on rapidity dependence of intensive quantities of multiplicity and net-charge distributions in

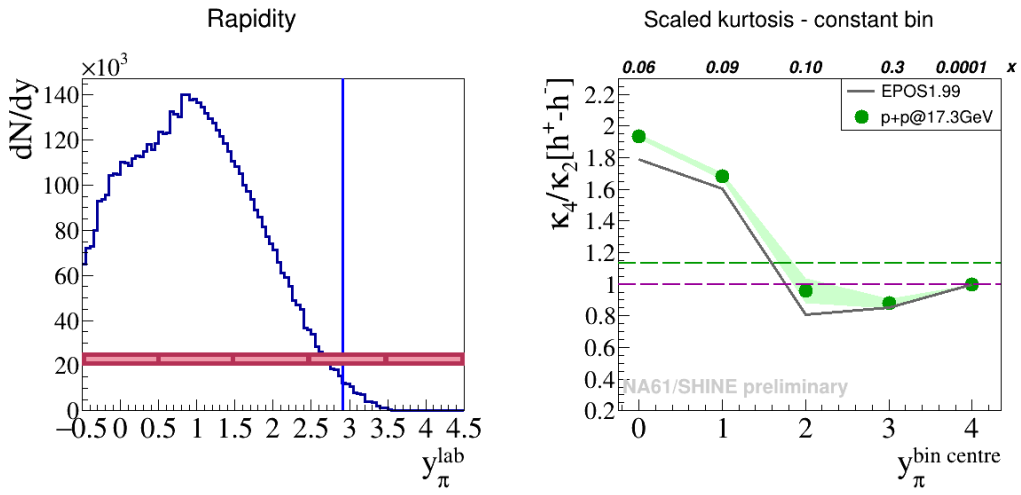

Figure 11: Definition of the rapidity bins (*left*) and preliminary results on rapidity dependence of fourth-order cumulant ratio of net-charge (*right*) in inelastic p+p collisions at 158 GeV/c. Rapidity y_π was calculated assuming pion mass. Statistical uncertainties are smaller than marker size, and the color band denotes systematic uncertainties. The dashed green line represents value in full analysis acceptance, and the dashed violet line corresponds to the Skellam reference value.

inelastic p+p interactions at 158 GeV/c were shown in Refs. [57, 58]. An example of such dependence for the fourth-order cumulant ratio is presented in Fig. 11. These measurements allow establishing the baseline in search for the CP. The strongest signal is observed for mid-rapidity bins $y_\pi < 1.5$.

2.1.11 (CP) Preliminary results on higher-order moments of multiplicity and net-charge in (inelastic p+p and) central Be+Be and Ar+Sc collisions

New preliminary results on multiplicity and net-charge fluctuations in central Be+Be, central Ar+Sc, and inelastic p+p collisions were shown in Refs. [57–60]. Results were presented using intensive quantities, and in the case of A+A collisions, they were limited to very central (0–1% centrality bin) interactions. Such narrow centrality selection allows to reduce volume fluctuations which could affect the measured signal. Figure 12 shows that a considerable difference between p+p and Ar+Sc interactions is visible for the second-order cumulant ratio. This difference does not remain for higher-order moments. Decrease of $\kappa_4/\kappa_2[h^+ - h^-]$ observed by the STAR experiment [61] is not visible for collected systems and energies (see Fig. 13). Moreover, no significant non-monotonic behavior, suggesting a critical point, can be observed.

2.2 New results for neutrino and cosmic ray physics

The NA61/SHINE collaboration has a program of hadron production measurements for long-baseline neutrino oscillation experiments at FNAL and J-PARC. These measurements improve knowledge of the neutrino flux produced in accelerator-based neutrino beams.

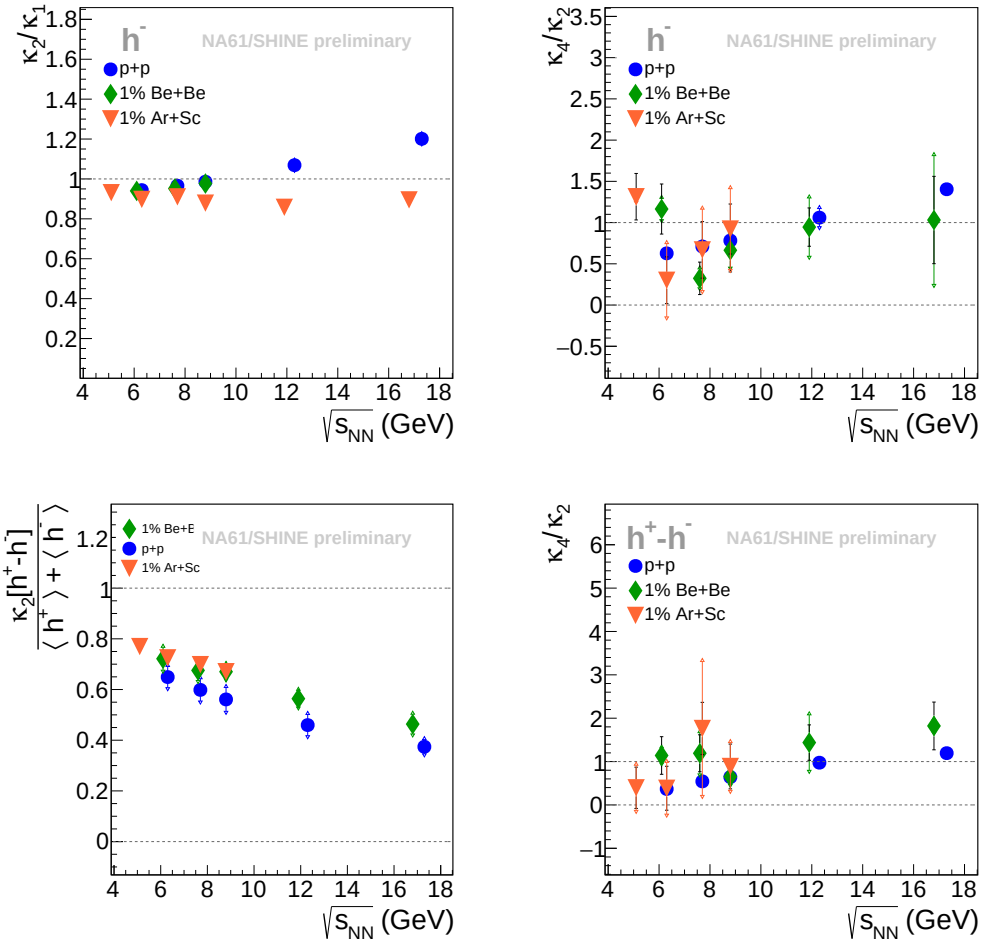

Figure 12: Preliminary results on system size (p+p, Be+Be, Ar+Sc) and energy dependence of multiplicity (*top*) and net-charge (*bottom*) fluctuations. Statistical uncertainties are presented as bars, the systematic ones as lines with arrows.

NA61/SHINE measures total cross sections and differential spectra of hadron yields from thin and replica neutrino beam targets. Furthermore, the collaboration performs hadro-production measurements relevant for the interpretation of air-shower data at ultrahigh energies and measures fragmentation cross sections for the understanding of Galactic cosmic-ray data.

2.2.1 Production cross section of p+C interactions at 31 GeV/c for T2K (J-PARC)

The production cross-section of 30.92 GeV/c protons on carbon has been measured by the NA61/SHINE spectrometer by means of beam attenuation in a copy (replica) of the 90-cm-long target of the T2K neutrino oscillation experiment. The corresponding results have been published recently [62]. Our method for direct production cross-section estimation minimizes model corrections for elastic and quasielastic interactions. The production cross-

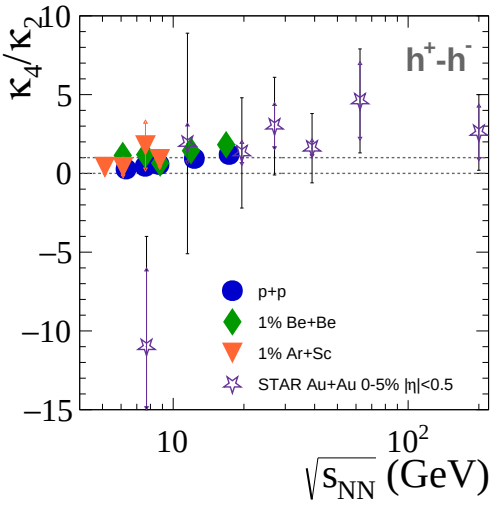

Figure 13: Comparison of the net–charge fourth-order cumulant ratio obtained in NA61/SHINE and STAR [61] experiments.

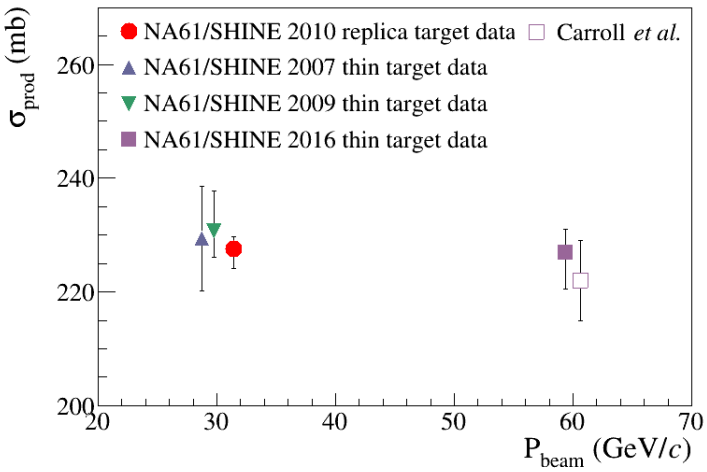

Figure 14: The result of the recently published long-target analysis [62] (red filled circle) compared to the production cross-section measurements for p + C interactions at different beam momenta. Alongside the previously published NA61/SHINE thin-target results, production cross section by Carroll *et al.* at 60 GeV/c [63] is shown.

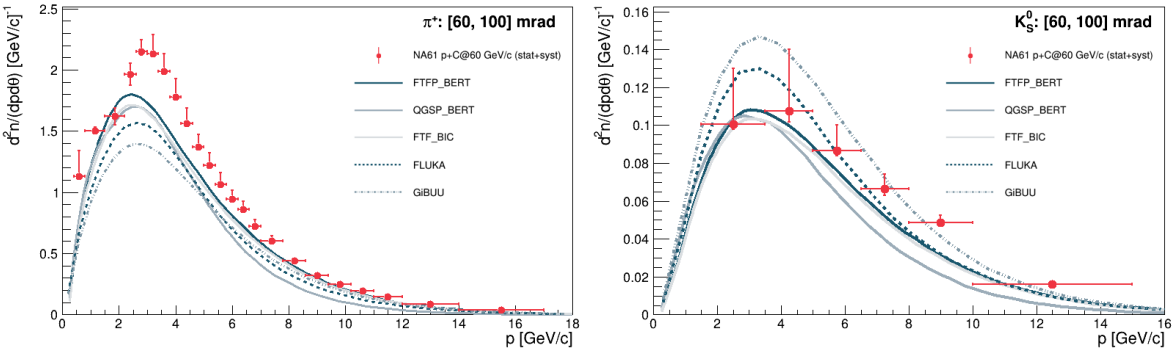

Figure 15: Examples of hadron spectra measured in p+C interactions at 60 GeV/c. The results are compared with various model predictions. (Left) π^+ yields for 60-100 mrad bin as a function of hadron momentum. (Right) K^0_S yields for 60-100 mrad bin as a function of hadron momentum.

section result is

$$\sigma_{\text{prod}} = 227.6 \pm 0.8(\text{stat})^{+1.9}_{-3.2}(\text{sys}) - 0.8(\text{model}) \text{ [mb]}.$$

It is in agreement with previous NA61/SHINE results obtained with a thin carbon target while providing improved precision with a total fractional uncertainty of less than 2% (Fig. 14). This direct measurement will reduce even further the uncertainty of the T2K neutrino flux prediction.

2.2.2 Hadron spectra in p+C and p+Al interactions at 60 GeV/c (FNAL)

The differential yields of neutral V^0 particles (K^0_S, Λ, $\overline{\Lambda}$) and charged particles ($\pi^\pm$, $K^\pm$, p, $\overline{p}$) from the interactions of 60 GeV/c protons on carbon and aluminum targets have been measured. Examples of differential yield measurements are shown in Fig. 15. These measurements are compared with several model predictions and will be used for precise neutrino flux calculations, particularly for Fermilab long-baseline neutrino beamlines. Analysis has been completed, and a publication on the results is under preparation.

2.2.3 Hadron spectra in p+C interactions at 120 GeV/c (FNAL)

In 2021, the first hadron production measurements using the FTPC system were performed. Differential multiplicity measurements of $\pi^\pm$, $p/\bar{p}$, and $K^\pm$ production via dE/dx analysis were completed, and differential multiplicity measurements of K^0_s, Λ and $\bar{\Lambda}$ via V^0 analysis were finalized. The results of the V^0 analysis are used to reduce systematic uncertainties associated with weak neutral decays in the charged particle analyses. The use of the FTPCs enables production multiplicity measurements at low angles and high momenta. Example pion, proton, and Λ spectra obtained in the very forward region can be seen in Fig. 16. Two complementary data sets, taken in 2016 without the FTPCs and in 2017 with the FTPCs, were analyzed. Their results were combined in regions of phase space with multiple measurements.

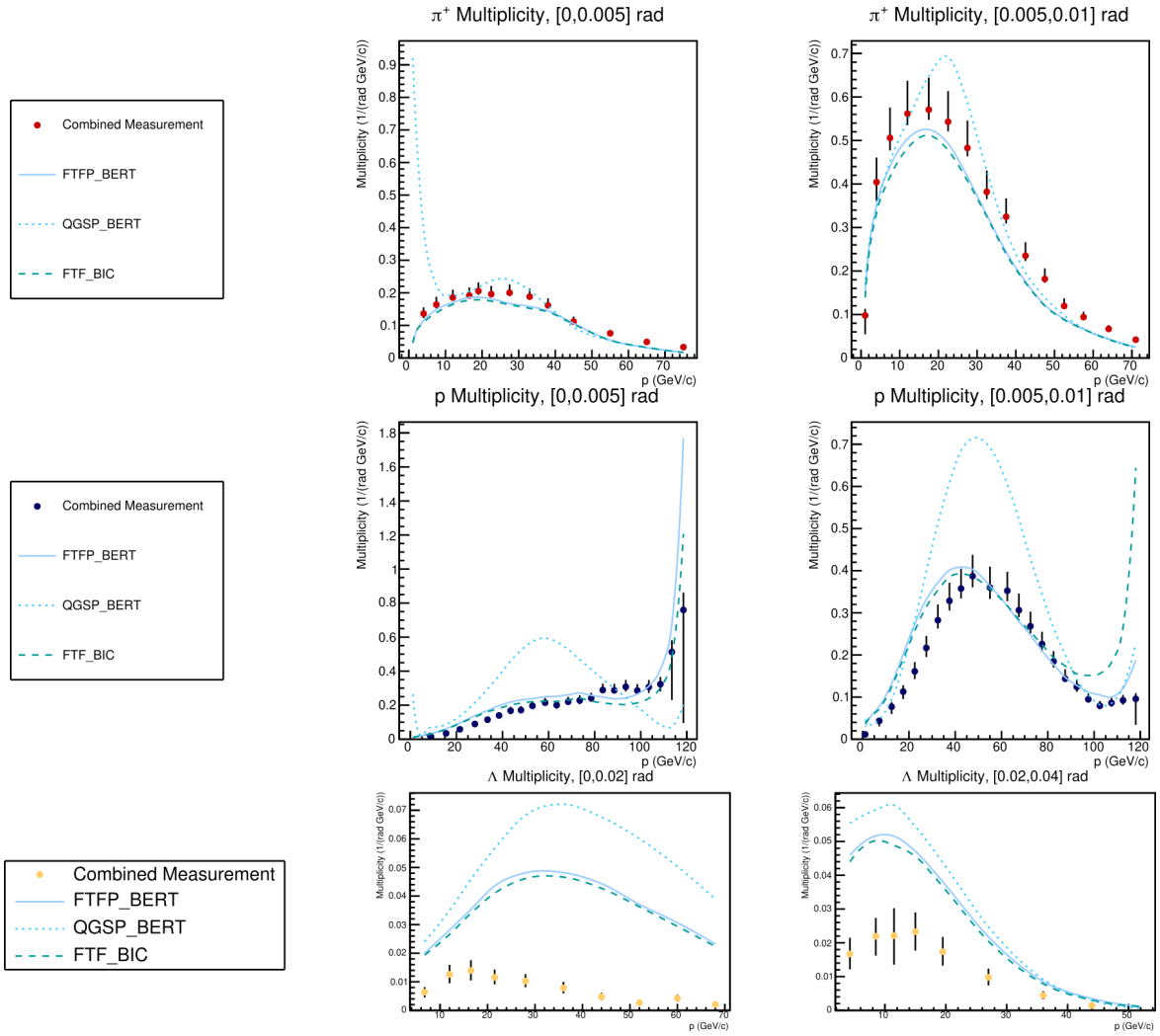

Figure 16: Examples of hadron spectra measured in p+C interactions at 120 GeV/c. Discrepancies can be seen between the measurements and various model predictions. Top: π^+ multiplicity in the two lowest angular bins. Middle: Proton multiplicity in the two lowest angular bins. These low-angle bins benefit significantly from the addition of the FTPCs. Bottom: Λ multiplicity in the two lowest angular bins. *Combined measurement* refers to the combination of the 2016 and 2017 multiplicity measurements.

These new measurements are important to both current and future FNAL long-baseline neutrino oscillation experiments. The 120 GeV/c p+C interaction is the primary reaction for neutrino creation in the NOvA beam, and it is foreseen to be the primary reaction used to produce the DUNE neutrino beam. Precise measurements of these particle multiplicities will allow DUNE to reduce systematic uncertainties associated with neutrino beam production by reducing reliance on Monte Carlo simulations to model the neutrino beam properties.

Work is underway to extend this analysis to include the forward time-of-flight walls. This will improve the particle identification at low momenta.

2.2.4 Hadron production in NOvA replica target (FNAL)

In 2018, data were collected with a 120 GeV/c beam on a replica of the long target used to generate neutrinos in the NuMI beamline at Fermilab for the NOvA long-baseline neutrino experiment. This target has a complicated shape that lacks azimuthal symmetry, so geometrical acceptance and binning studies are considerable challenges in the analysis. These studies were underway during 2021. Calibration of the data set is nearly complete. This work will further improve flux estimates for NOvA and MINERvA, and it will also lay the groundwork for analyzing future similar data with a prototype of the target that will be used in the DUNE experiment.

2.2.5 Fragmentation cross-section for Galactic Cosmic Rays

New results on the nuclear fragmentation of carbon in C+p interactions were presented in Ref. [64] using data from the 2018 pilot run [65] on the feasibility of nuclear fragmentation measurements relevant for galactic cosmic rays. This analysis extends the previous results on B production [66] to measure the production cross section of ^{11}C production in ^{12}C-p interactions. For this purpose, carbon isotopes need to be identified (cf. left panel in Fig. 17) and the C+p reaction cross section is determined by subtracting C+C interactions from C+CH_2 interactions. The result is shown in the right panel of Fig. 17). Even though the pilot run lasted only 3 days, the result already adds information to the existing world data, clearly establishes the possibility of fragmentation measurements with NA61/SHINE, and provides important insights for the physics data taking foreseen during the coming years (see Sec. 5).

2.2.6 Galactic Anti-Nuclei

Studies of the formation of light anti-nuclei (in particular, anti-deuterons) in nuclear collisions aim to understand the background to searches for Dark Matter in the Galaxy. The production of anti-nuclei in hadronic interactions is not well understood. The predicted anti-nucleus fluxes from cosmic-ray propagation models are highly correlated with antiproton production in proton-proton interactions. Hence, high-precision antiproton production cross sections at different collision energies near the production threshold of different light anti-nuclei are very important [67–69].

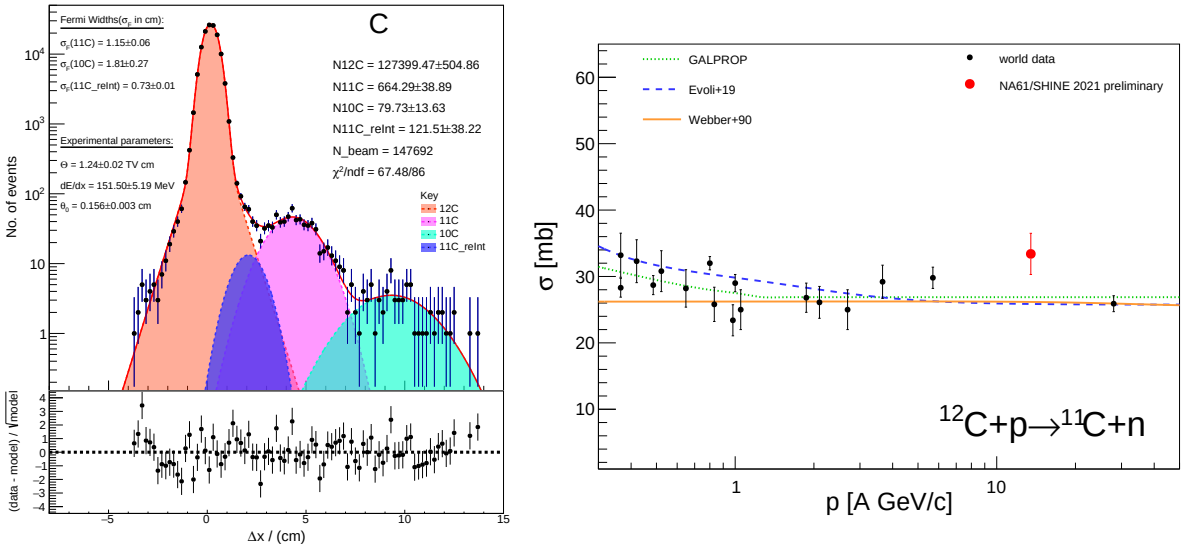

Figure 17: Left: Fit of carbon-isotopes in C-C interactions indentified via the relative bending Δx with respect to the beam in the MTPC; right: preliminary ^{11}C production cross section compared to previous measurements and model predictions [64].

2.2.7 Preliminary results on π^+, π^-, K^+, K^-, p, $\overline{p}$ production in inelastic p+p collisions at 158 GeV/c using the combined p+p large data set.

The large, combined p+p data sets at 158 GeV/c contain about 60 million collision events, recorded during years 2009, 2010 and 2011. The main goal of the dE / dx-based analysis is to produce high-precision (anti)proton spectra, along with kaon and pion spectra as well. The preliminary transverse momentum particle spectra in rapidity slices for positively and negatively charged protons, kaons, and pions produced in inelastic p+p interactions at 158 GeV/c are presented in Fig. 18 along with previously-published results in Ref. [6] from the analysis of only the 2009 p+p data set. The new results are able to reduce the statistical uncertainties, as well as extend the transverse momentum region to 1.5 GeV/c.

The time-of-flight analysis of these data sets to investigate deuteron production is currently underway. Along with angular correlations of these particle productions, these results will be used to further improve and tune hadronic generators like EPOS-LHC. About 9 million p+p collision events at 400 GeV/c from 2016 are also in the process of being analyzed.

A preliminary analysis on (anti)deuteron and antiproton production in p+C collisions at 31 GeV/c data taken in 2009 is ongoing. A novel approach to estimate the contribution of secondary deuterons produced in such collisions in a restricted area of phase-space has been developed and a performance study gave promising results for deuterons. As for antideuterons and protons the statistics of tracks is too poor to allow for any inference. The method is based on a data-driven correction for the contribution of secondary deuterons produced in target and an implementation of the coalescence model in MC-generated events in order to estimate the geometric correction.

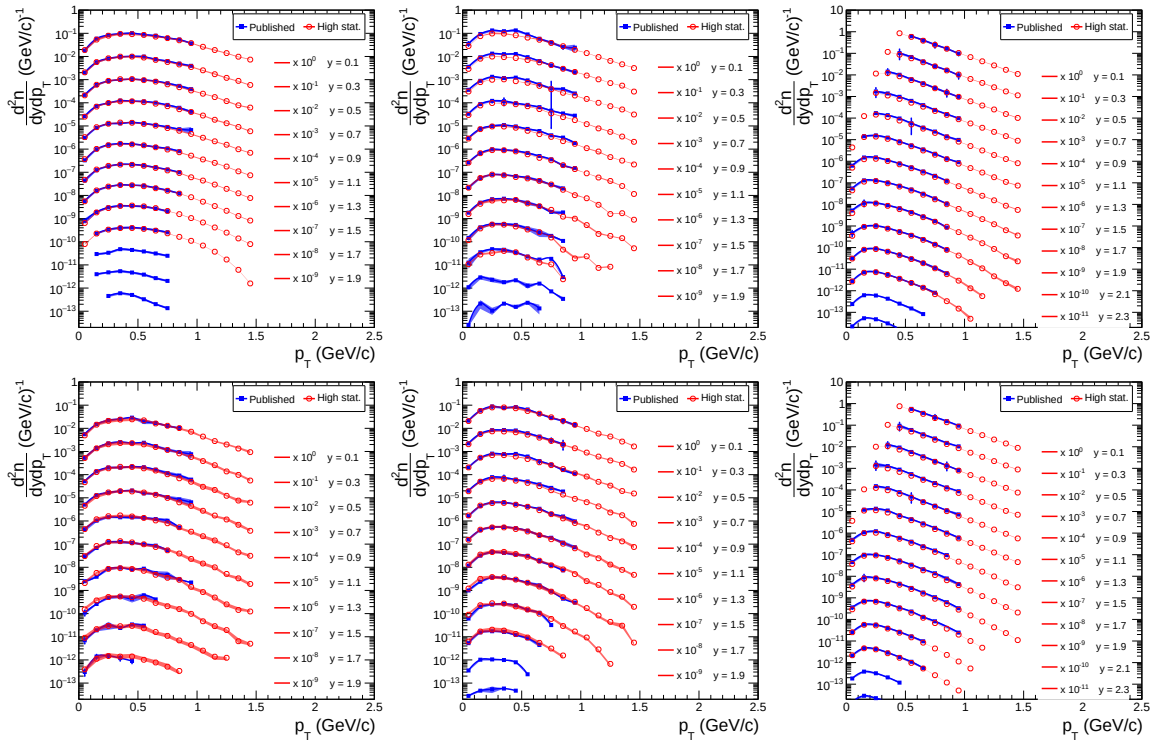

Figure 18: Transverse momentum particle spectra in rapidity slices for positively (top) and negatively (bottom) charged protons, kaons, and pions produced in inelastic p+p interactions at 158 GeV. New preliminary results from the large, combined p+p data set at 158 GeV/c is shown in red, and the previously-published results in Ref. [6], from the analysis of the 2009 p+p data set are shown in blue. Shaded bands show systematic uncertainties.

3 Software and calibration upgrades

As was reported in past status reports, NA61/SHINE has migrated its software from the "Legacy" framework to a new software framework, called SHINE. Since we have stopped using the Legacy software and some core components have been implemented into the SHINE framework, this section will focus on the SHINE framework.

3.1 SHINE software

3.1.1 SHINE framework

Since the previous status report, two software releases were made. Most of the changes were associated with further development of the Monte Carlo simulation and event reconstruction. For the Monte Carlo simulation, GEANT4 version 10.7 has been implemented instead of version 10.4 as was previously used. The Kalman Filter-based tracking algorithm reported in last year's Status Report has been implemented for the event reconstruction. Performance

comparison is underway against the Legacy reconstruction. In addition, Forward Time-of-Flight (F-TOF) and Vertex Detector (VD) software have been developed and are described in the following paragraphs.

There have been several pieces of software written for the F-TOF wall. As the F-TOF has used DRS4 readout electronics since 2017, software to calibrate the DRS4 signal traces was integrated into the SHINE framework. In addition, for the 2017 and 2018 datasets, the F-TOF raw event files are stored separately from the central DAQ data. A new module was written to match the 2018 central DAQ events to the F-TOF events, and a matching procedure is being worked on for the 2017 data, which has dropped F-TOF events and asynchronous event files. Two of the four total calibration stages for the F-TOF have been written so far. The scintillator bar position calibration and the signal propagation speed calibration were incorporated into a module. The calibration of PMT T0's and the start signal timing at the S1 counter have not yet been completed.

Because of high statistics open charm production data collected in Pb+Pb collisions with an upgraded VD, an update of the VD software has started. In particular:

(i) Up to now, the VD software was implemented as a standalone code, so the first steps concern its integration into the SHINE software. Managers handling the setup of the VD during simulation/reconstruction have been updated. VD geometry configurations have been moved to the SHINE Database, enabling one to produce MC simulations for the runs in 2017 and 2018 with the VD in operation. VD reconstruction code was integrated into the build system, and thus corresponding modules are now available for all users of SHINE software.

(ii) As the primary goal of the VD is to measure open charm production, the code was highly optimized for the reconstruction of short-lived D^0 mesons. However, as a consequence, reconstruction of secondary tracks originating several millimetres downstream the target suffers from inefficiency. To overcome this issue, an adaptation of the tracking algorithm implemented in the SHINE software for TPC reconstruction is in progress.

3.1.2 Software for the upgraded detector

Detector hardware upgrades necessitate many software upgrades to maintain software compatibility. The upgraded TPC electronics deliver data in a new raw data format, and corresponding decoding and parsing software infrastructure must be available in the SHINE Offline Framework. During the TPC electronics testing in July and September 2021, a detector raw data parser was written and used for the quality assessment of TPC raw data. This parser will be moved into the Offline Framework I/O libraries. A second parser was written to translate raw TPC front-end electronics channels to physical TPC pad objects, a crucial step toward data reconstruction.

Similar raw data parsing software is present for the DRS4 raw data. The newly-implemented `evt::raw::DRS4Trace` class, implemented as the base class for all DRS-based detectors, will be filled by the DRS4 raw data parsing software. The parser is planned to be moved into the Offline Framework I/O libraries in October 2021.

3.2 Calibration

Calibration activities and upgrades during last year are:

(i) The procedure for magnetic field calibration based on $\pi^+\pi^-$ (K^0_s decay) and $\pi^- p$ (Λ decay) invariant mass distributions was significantly improved. The modified procedure is now much more effective (less time-consuming) in processing large numbers of events.

(ii) The TPC drift velocity, time constants, and the alignment of TPC detectors were calibrated for all Xe+La data samples as well as for Pb+Pb collisions at 150A GeV/c.

(iii) The TPC dE / dx calibration software package was supplemented by the automation scripts. The procedure was additionally tested on p+Pb data samples and is in preliminary use for Xe+La data samples.

(iv) The new approach for the Main and Forward Projectile Spectator Detector (PSD) calibration with cosmic muons was formulated and used. The first calibration on the proton beam was done.

(v) The Vertex Detector software, including the calibration procedure, was implemented in the SHINE software framework. The software was tested on newly calibrated data.

(vi) The new bookkeeping system was prepared and used for current calibration tasks.

4 Hardware upgrade

During the Long Shutdown 2 at CERN (2019-2021), a significant modification of the NA61/SHINE spectrometer was ongoing. The upgrade has been motivated by the charm and neutrino programs, both of which require a tenfold increase of the data-taking rate to about 1 kHz. The charm program also requires doubling of the phase-space coverage of the Vertex Detector. This, in particular, requires the following:

(i) construction of a new Vertex Detector,

(ii) replacement of the TPC readout electronics,

(iii) implementation of a new trigger and data acquisition systems,

(iv) upgrade of the Projectile Spectator Detector,

(v) construction of new ToF detectors for particle identification at mid-rapidity.

The upgrade is well advanced but unable to be finished in time as established in the schedule. Due to a combination of Covid-related obstacles (shortage of electronic components, delayed production of hardware, and travel restrictions), not all detectors are fully upgraded yet. We have achieved many milestones of the upgrade, such as:

(i) Implementation and test of the data acquisition system that is fully scalable and allows an easy way to extend the experimental system with a new detector. This functionality was never reached in the old DAQ system.

(ii) Test and commissioning of the trigger system.

(iii) The implementation and test of the readout system are based on the DRS4 chip, where the entire waveform will be measured and stored.

(iv) Testing and commissioning of the PSD calorimeter with new readout electronics.

(v) Testing of new Beam Position Detectors (BPD) using a single-sided silicon detector.

The upgrade of the majority of the detector's subsystems will be finished by the end of 2021, and the upgrade of the entire detector will be finalized by early spring of 2022.

4.1 Vertex Detector

The primary purpose of the VD is to provide precise information on particle tracks close to the target. This information allows separation of primary and secondary vertexes even for such short-lived probes as open charm mesons. NA61/SHINE experiment used a pilot version of the VD, the so-called Small Acceptance Vertex Detector (SAVD), during the test measurements in 2017 for Xe+La at 150A GeV/c and in 2018 for Pb+Pb at the same beam momentum. These measurements have shown that the measurement of D mesons at the SPS energy domain in fixed-target experiments can be realized. However, precise measurement of open charm with the SAVD was not possible due to small acceptance of the device [70].

During the LS2 period, NA61/SHINE is upgrading the SAVD detector to a high acceptance device to permit precise open charm measurements from 2022 to 2024. The main part of the upgrade is related to the replacement of the MIMOSA-AHR sensors used in SAVD to modern ALPIDE sensor-based modules (staves) developed by the ALICE ITS project. The replacement will increase the acceptance of the device and increase the data taking rate from 80 Hz to the a0nticipated 1 kHz.

In 2021 the efforts of the NA61/SHINE VD group were focused on the adaptation of the ALICE ALPIDE readout system, based on the MIMOSA boards, to the needs of NA61/SHINE. Because only five sensors (out of nine) will be located in the acceptance of NA61/SHINE, a dedicated adapter board was developed that allows one to control and read data from two staves connected to one MOSAIC board only (see Fig. 19). Such a solution allowed us to reduce the costs of the final read-out system significantly. In the period of October and November 2021, a first test on the beam of the upgraded Vertex Detector will be performed with the VD local readout system integrated with the new NA61/SHINE central DAQ and with the mechanical infrastructure modified to account for hosting of the ALICE ITS staves and feed-through related to the new readout system. A large part of the mechanical elements of the SAVD device will be re-used.

4.2 Time Projection Chambers

A replacement of the entire readout electronics, necessary for increasing the readout rate to 1 kHz, has beeb started using the former ALICE TPC readout electronics. For connecting the ALICE front-end cards (FECs) to the NA61 wire chambers, new adapter boards were

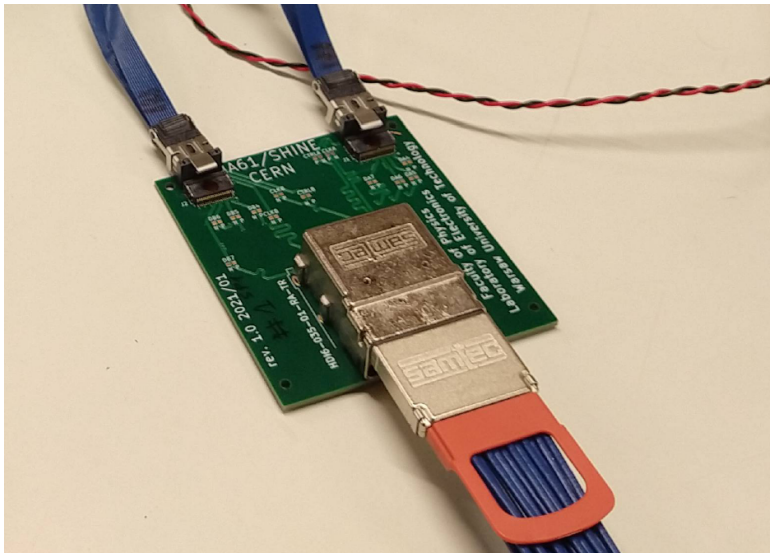

Figure 19: Dedicated adapter board. On one side, the board is connected to two ALICE ITS staves with visible firefly cables, and on the opposite side, it is connected to the MOSAIC board.

developed that include protection circuitry to prevent discharges in the wire chambers from damaging the charge sensitive input stages.

In Fig. 20 (left) the new layout is shown for the MTPC standard resolution chambers.

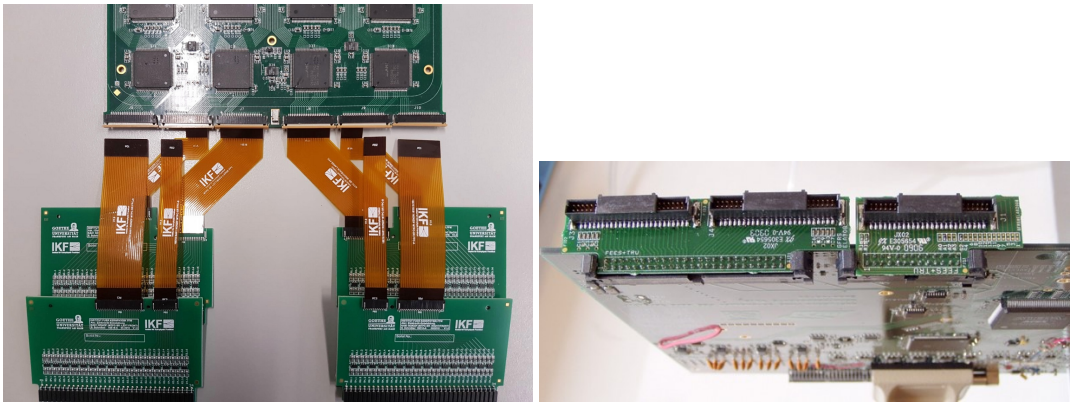

Figure 20: Layout of the new readout electronics showing the adaptation of the ALICE front-end card to the NA61 wire chambers for the Main TPC (MTPC) standard resolution chambers using 4 adapter boards (*left*). New output adapter for the transition between the two output connectors of the FECs and the 3 ribbon cables of the cable bus connecting to the RCU2 (*right*).

For topological reasons the connection between FECs and Readout Control Units-2 (RCU2) had to be adapted to accommodate relatively large distances of up to 2 m. For this an output adapter board was developed, also shown in Fig. 20 (right) allowing us to use standard ribbon cables with proper impedance matching.

This new readout configuration is in the process of being installed in all TPCs, as described below.

4.2.1 Vertex TPCs

After moving the Vertex TPCs (VTPC) out of the magnets to allow access, the old electronics was removed and the new electronics was mounted following the scheme described in the 2019 status report.

After the installation of the FECs with 128 readout channels each (41472 channels in total for both VTPCs), they were tested for noise and connectivity.

Figure 22 shows the noise distribution for the two VTPCs separately. The mean value was found to be 0.926 ADC channels and 0.937 ADC channels excluding the first two pad-rows in VTPC-1 and VTPC-2, respectively. In these two pad-rows the length of the input Kapton cables had to be doubled to accommodate the first FECs of each FEC-row on top of the mounting frame of the wire chambers, illustrated in Fig. 21.

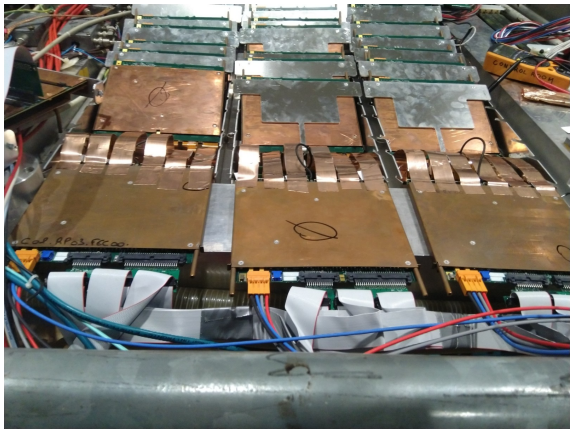

Figure 21: For the connection of the first row of FECs much longer Kapton cables with a copper shielding foil were used.

This led to a pickup of high frequency noise. Shielding of the Kapton cables by copper tape improved the situation considerably. Nevertheless, the noise compared to the other readout channels is elevated by about 3 ADC channels. In general the noise level is higher than in ALICE due to the fact that additional noise is introduced by the protection circuitry and the trace length on the adapter circuit boards. In VTPC-2 the noise level is slightly higher compared to VTPC-1 caused by higher noise in sector 6 due to the fact that there is a capacitive decoupling introduced. This was necessary since the pad plane was sprayed with a slightly conductive layer of MoS2 already in the original NA49 setup.

The connectivity to the readout chambers was tested using the NA61 calibration pulser system. For the tests described above the LV system (Wiener PS) in its final setup was used (see Fig. 23).

The upgraded cooling system with its new chiller unit was connected and tested successfully. The new gating grid pulser system, taken over from the ALICE experiment, was configured and tested. It includes 6 new power supplies PMX500-0.1A from the Kikusui company allowing for offset voltages down to -400 V (at the bottom of the left rack). An overall view of the gate pulser system together with the LV system is shown in Fig. 23

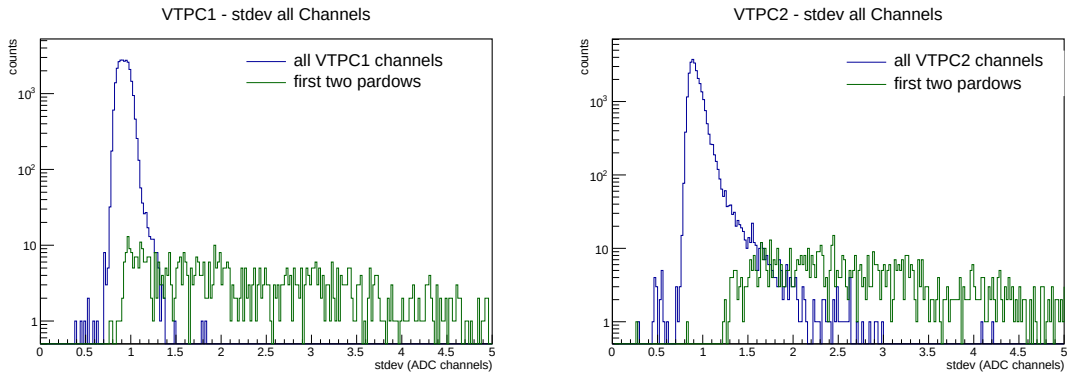

Figure 22: Noise distribution in VTPC-1 (*left*) and VTPC-2 (*right*) with and without the first two pad rows.

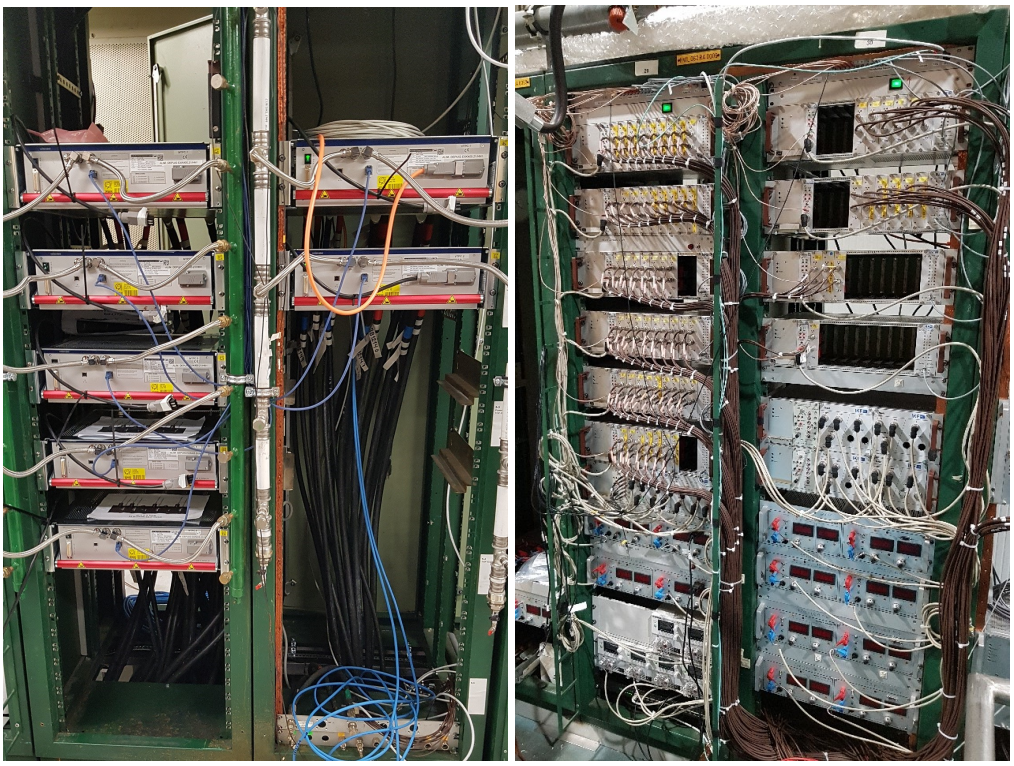

Figure 23: The new Low Voltage system consisting of 7 water cooled Wiener PL512 power supply modules mounted in MARA crates (*left*). Right: New gating grid pulser system (*right*) . Both systems supply all TPCs.

The HV system was tested at a reduced voltage.

Figure 24 shows the two vertex TPCs after completion of the upgrade ready to be moved back into the magnets.

Figure 24: VTPC-1 and VTPC-2 ready to be moved back into the magnets. The cooling hoses on both sides of the TPCs are visible as well as the LV cables. The ribbon cables connect the FECs to the RCU2s mounted at the upstream and downstream ends of the TPCs.

4.2.2 Main TPCs

The mechanics to mount the FECs was installed together with the input adapter cards on all 50 sectors of the two MTPCs.

Several sectors are already equipped with FECs. In Fig. 25 a high resolution sector is shown with all FECs installed. The LV bus bars and the cooling plates are not yet in place.

The cables for the LV supply of the two main TPCs are installed including the 10 patch panels close to the TPCs for the transitions to the local patch cables connecting to the bus bars inside the sectors.

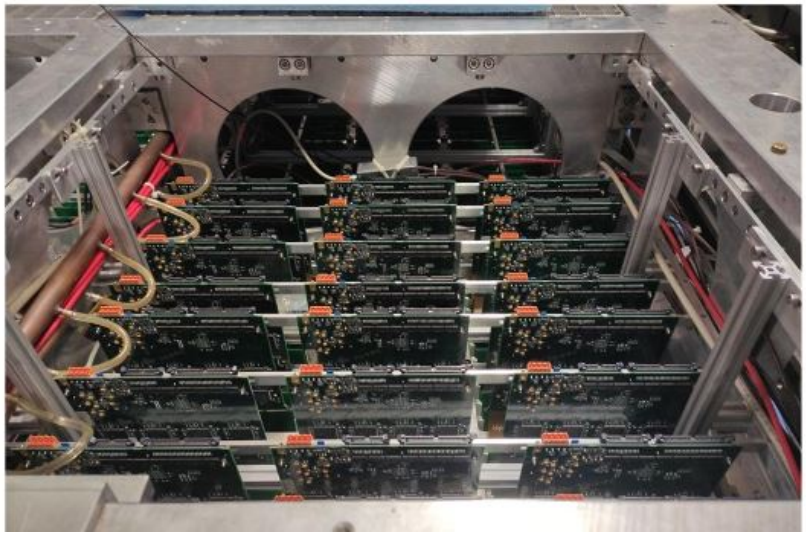

Figure 25: A high resolution sector of the MTPC-L with all FECs installed. The LV bus bars and the cooling plates are not yet in place.

4.2.3 Gap TPC

Due to space restrictions the 8 FEcs for the read-out of the Gap TPC were mounted horizontally in two stacks above the TPC inside the support frame, shown in Fig. 26. Only half of the 128 channels is used in the 4 FECs mounted on the left side. The Kapton cables are not yet installed due to a delay in production.

Figure 26: Top plate of the GAP TPC with the 8 FECs mounted and the input adapters plugged in. The Kapton cables are not yet installed.

4.2.4 Forward TPCs

The FTPCs have been prepared for the installation of the new FECs. For this purpose scaffolding was installed. The new electronics will be installed and commissioned before the end of the 2021 run.

4.3 Time-of-Flight detectors

The new ToF system based on the BM@N-type [71] multi-gap resistive plate chambers (MRPC) [72] has been offered as a substitution for the previous system. A scheme of the MRPC detector is shown in Fig. 27. The new ToF detectors are assumed to provide performance similar to the existing ToF-L/R detectors. Therefore, requirements for the new ToF system should be as follows:

(i) high efficiency $> 95\%$;

(ii) time resolution < 75 ps;

(iii) high granularity to keep the overall system occupancy below 10%;

(iv) position resolution ≈ 10 mm to provide efficient matching of the ToF hits with the reconstructed tracks;

(v) low power dissipation in proximity to the TPCs.

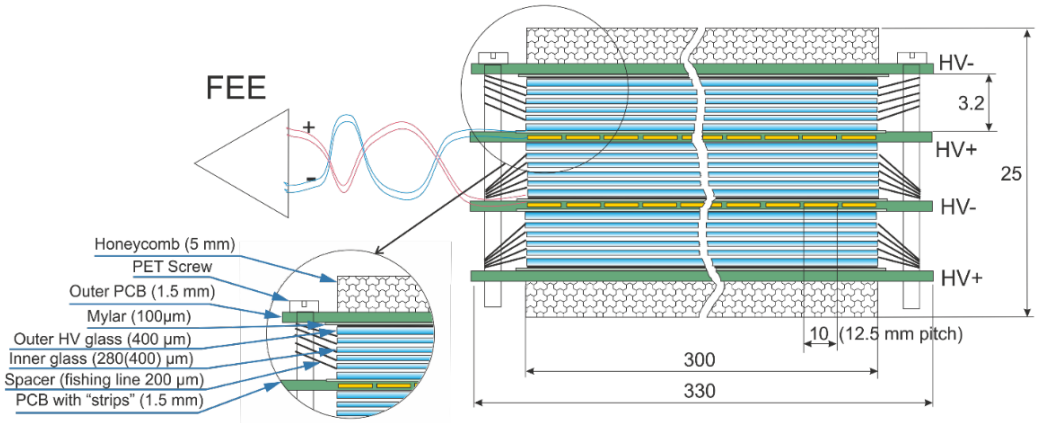

Figure 27: Schematic cut view of the MRPC with the triple-stack architecture

The new front-end boards were designed in the alternative analogue front-end (AFE) configuration in comparison with the BM@N readout electronics on the NINO and HPTDC chips [73,74]. The motivator to choose the above readout was the existing NA61/SHINE DAQ system based on the 32-channel DRS4 modules and the fact that the new waveform digitization concept has advantages in providing additional information about signals and processes in MRPC comparing with the mainstream discrimination technique [75]. The AFE module has been designed in a cascade structure. The first cascade of AFE was realized on the 6 GHz differential amplifier ADL5565 [76]. The second cascade consisted of a 1 GHz low distortion amplifier AD8009 [77]. The usage of the AD8009 was motivated by the construction of the DRS4 module. Additionally, to compensate for the signal losses, the second cascade was designed as a circuit of an active cable on the DRS4 module side.

The beam test of the produced MRPC with an analogue readout was carried out at accelerator S-25R "PAKHRA" in the Lebedev Physical Institute of the Russian Academy of Sciences (LPI RAS), Troitsk, at the end of 2020. The positron beam in the transverse direction

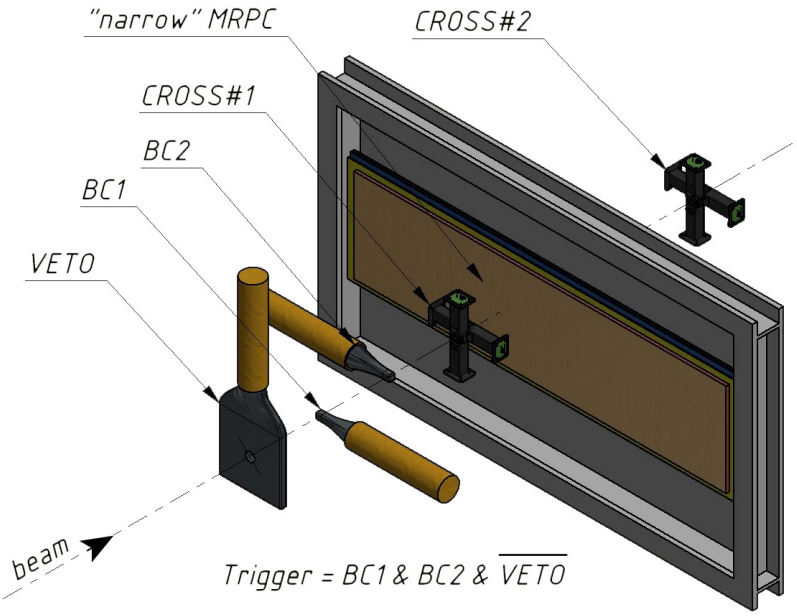

Figure 28: Schematic view of the setup of the MRPC prototype beam test with the analogue readout in Troitsk

to the chamber was supplied with the momentum of 300 MeV. A schematic of the experimental setup is shown in Fig. 28. The trigger system consists of a set of scintillators (BC1, BC2 plus veto counter VC with a hole for beam particles), which are read out by photomultiplier tubes (PMTs). The set of the counters define the area of 1.0x1.0 cm^2 of the beam. An additional set of four scintillators (CROSS#1.0, CROSS#1.1, CROSS#2.0 and CROSS#2.1) was used as a reference. Each scintillator counter has dimensions of 100x10x10 mm^3. The light from the scintillators was registered by SiPMs from both sides. The reference counters were grouped into two identical crosses (CROSS#1 and CROSS#2). The time resolution of each cross, obtained in ToF measurements was approximately equal to 40 ps. The "narrow" MRPC with the active area of 150×600 mm^2 was chosen as a detector for testing. The tested MRPC was located between two crosses on a positioning device that could move remotely in the X-Y plane to perform detailed area scans of the detector. All the detectors were aligned with respect to the beamline and defined a small (10x10 mm^2) area of the beam. The signals from the MRPC were amplified by the AFE from both sides of the strips. The output pulses from the AFE as well as SiPM were digitized by the DRS4 board.

The efficiency and time resolution were scanned as a function of the applied high voltage for a low particle flux of about 15 $cm^{-2}s^{-1}$. The voltage was in the range of $11 - 12.75$ kV. The results are demonstrated in Fig. 29 (*left*). The best time resolution achieved at 11.75 kV was equal to $\approx$ 52 ps. The efficiency was 99%. The time resolution was calculated as a solution of the system of linear equations for the time differences of the detector and crosses. The efficiency of the MRPC was measured by analyzing its response at the presence of the signals from both crosses. If at least one strip is fired, the detector is considered to be efficient.

The positioning device allowed us to move the detector along the X and Y directions with an accuracy of 0.5 mm. The investigated MRPC was moved practically along its length, changing its position relative to the particle beam and other reference detectors. The measured

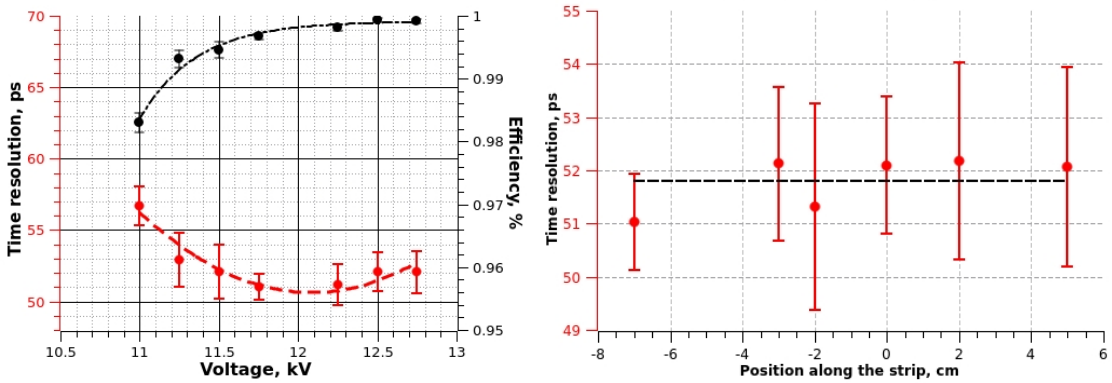

Figure 29: Efficiency and time resolution of the MRPC prototype with the analogue readout (*left*). Dependence of time resolution on the position of particles along the strip (*right*)

time resolution along the strip is presented in Fig. 29 (*right*).

After successful tests of the MRPC prototypes, it was decided to organize a full production cycle of the MRPC detectors. The detector assembly technology consists of several stages. The first step, glass cleaning, is performed in an ultrasonic bath with a special surfactant. The glasses are washed with deionized water, purified by a reverse osmosis filter in a special cleaning system. After washing, the glass is dried in a special drying oven, after which it is conveyed to the detector assembly area or the conductive paint area. The second stage is the automatic application of semiconductive enamel on the glass and its subsequent drying. The final part o the detector assembly work is performed in a cleanroom (ISO 7). The cleanroom houses the levelling tables with granite slabs to ensure the precision flatness of the detectors and ensuring the glass spacing is accurate to better than 10 µm.

The assembled detectors are also inspected in several steps:

(i) optical quality control of the MRPC assembly using a microscope with an automatic displacement system.

(ii) high voltage testing of the MRPC (2 stages)

(iii) quality control of detector soldering

(iv) check of the differential line of the signal passing through the detector

Since the middle of last year, the MRPCs for the ToF-L were in series production. In total, during this period, twenty (20) "narrow" detectors with 150×600 mm^2 active area and seven (7) "wide" detectors with 300×600 mm^2 active area were manufactured. This number of detectors completely covers the needs for the ToF-L wall construction. At the end of this year, it is planned to assemble, install and commission the ToF-L system in the NA61/SHINE experimental hall.

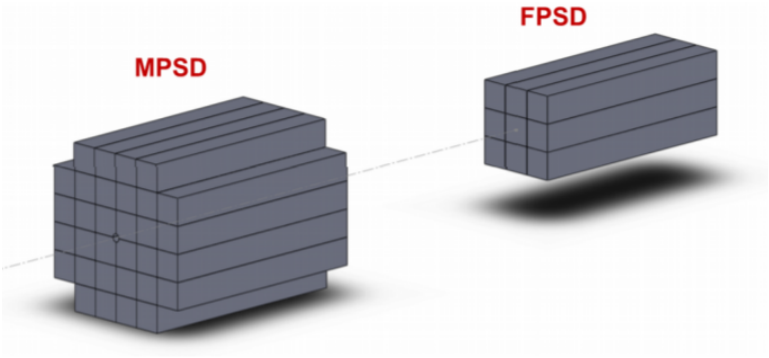

Figure 30: The PSD calorimeters schematic view.

4.4 Projectile Spectator Detectors

The main aim of Projectile Spectator Detectors (PSD) is to measure event centrality on an event-by-event basis and form a trigger decision based on the centrality. The PSD consists of:

(i) Main PSD (MPSD) - the old PSD of NA61/SHINE with the modified centre part, which has now a beam hole

(ii) Forward PSD (FPSD) - the 9 modules 20cm x 20cm assembly inside the radiation protection cave

The schematic of the detectors is shown in Fig. 30. During the hardware upgrade, the MPSD and FPSD were installed in the area. The MPSD and the FPSD are shown in Fig. 31. The new FPSD Frond-End electronics (FEE) has been designed, produced and mounted on the FPSD modules. The view of the FEE board is shown in Fig. 32. The read-out of the new PSD system is organized with new DRS4 boards with fast waveform reading. The DRS4 board is shown in Fig. 33. The new DRS4 read-out was tested in 2021 on the hadron and muon beams. The HV of photodiodes has been tuned to fit the dynamic range of DRS4. A new temperature gain compensation system was introduced to replace the old temperature control system, generating a lot of pickup noises. The waveform of one MPSD channel and muon spectrum was taken on muon beam is shown in Fig. 34.

4.5 Beam position detectors

The primary purpose of Beam Position Detectors (BPDs) is to measure beam particle trajectory on an event-by-event basis (particle-by-particle). The requirements for the detector include:

(i) Detector/detectors should work with p and Pb beams at momentum 13-150A GeV/c.

(ii) The detector should be able to measure the x and y position of each beam particle at each detector plane, with minimal pileup at the planned beam intensity of 100 kHz.

(iii) The precision of the position measurement should be on the level of 250 μm.

Figure 31: The MPSD and the FPSD installed in the area.

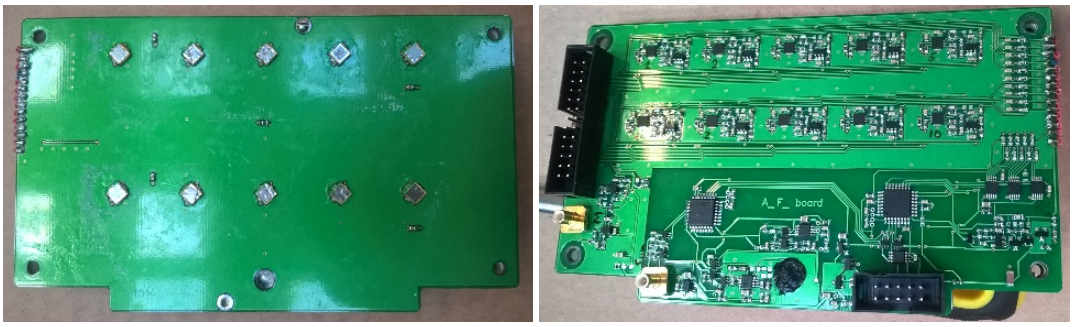

Figure 32: The FPSD FEE board.

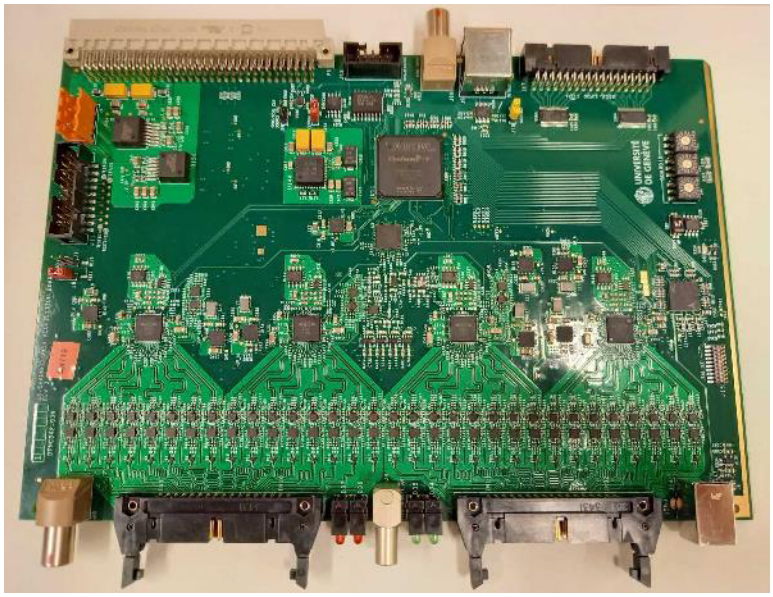

Figure 33: The DRS4 board for PSD read-out.

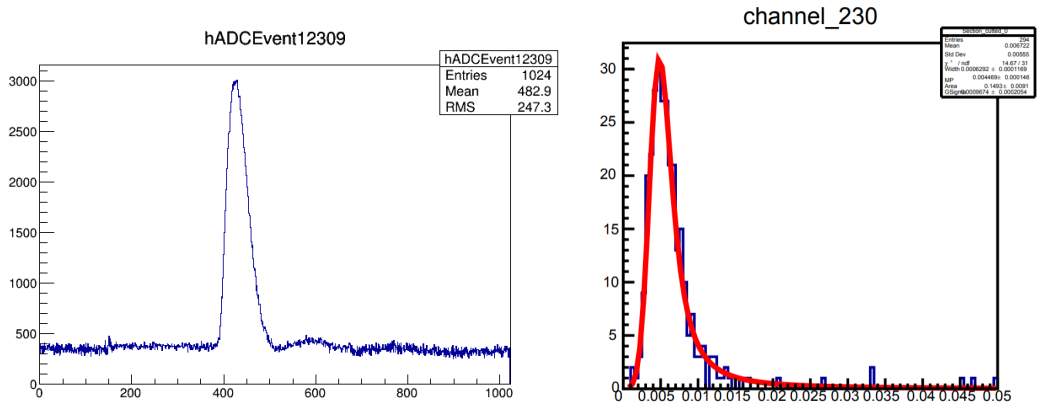

Figure 34: The MPSD waveform from one channel (*left*) and muon spectrum (*right*) obtained during the 2021 test beam period. The red line shows Landau+Gauss convoluted fit function.

obtained

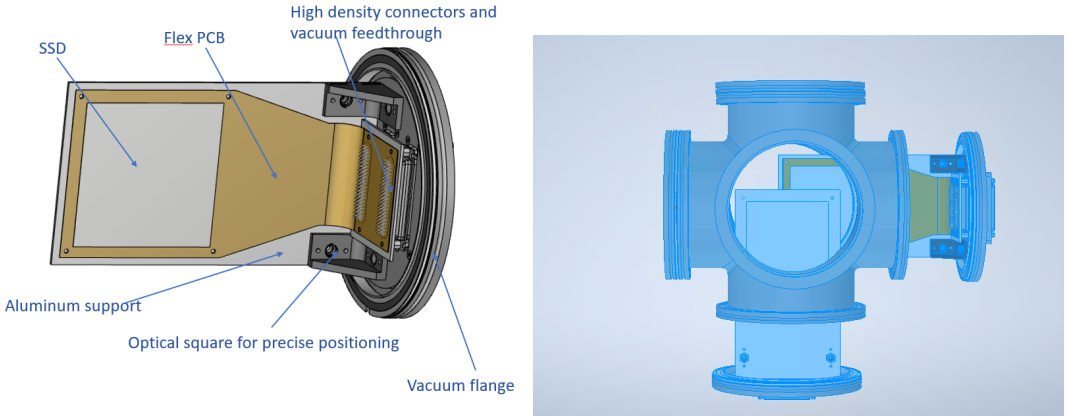

Figure 35: Rendering of the single-layer BPD detector (*left*). It consists of the SSD mounted to a flex PCB, an aluminum frame, and the vacuum flange. Signals are extracted via high-density connectors and vacuum-tight feed-throughs. The two single layers of the detector will be installed in the six-way cross in the vacuum (*right*).

(iv) The detector should operate in vacuum $\left(10^{-6}\right)$.

(v) Material in the beam should be minimized.

New BPDs were designed based on Si strip detectors (SSD). A Si photodiode with p-n junctions (particle detection structures) is several micrometres to several tens of micrometres in width arranged in a stripe formation. We are using Si strips produced by Hamamatsu, model S13804 [78]. Since the Hamamatsu Si strip has a 10x10 cm^2 active area and is bigger than the beam size, the readout will be limited to 200 central channels in each layer. It will provide an active area of about 5×4 cm^2.

The Si strip matrix is glued and bonded to a flex PCB and mounted to the vacuum flange. The signals are sent outside the vacuum pipe through high-density connectors. A rendering of the detector is shown in Fig. 35 (*left*). Two single detector layers will be installed in the six-way cross in the vacuum, as shown in Fig. 35 (*right*).

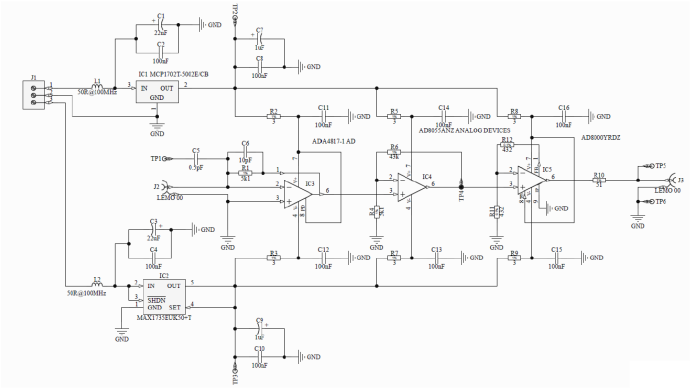

Figure 36: Single channel amplifier schematic for the BPDs.

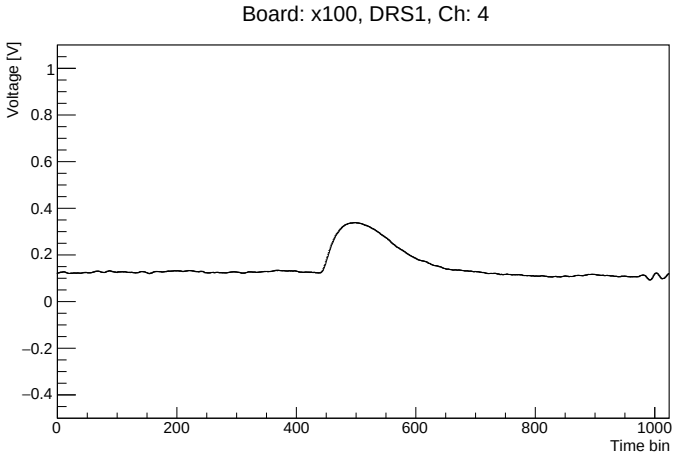

Figure 37: Signal from the protodype BPD readout by the DRS4 system at NA61/SHINE.

Outside the vacuum, analog amplifiers will be installed, and signals will be read out by the standard NA61/SHINE DRS4 system. The design of the single-channel amplifier is shown in Fig. 36.

A single-layer 15-channel prototype was developed and tested in August-September 2021 on h^+ beam. The prototype was supposed to read out only 15 strips. The test setup showed the proper operation of the detector: correlation with trigger signals and compatibility with the DRS4 readout system. Typical signals are above 250 mV. A sample signal from the BPD prototype readout by the DRS4 system is shown in Fig. 37. The complete setup of the BPD system is under production and expected to be complete around the beginning of November.

4.6 Trigger and Data Acquisition System

A barrack in the north area has been dedicated for the new Trigger and Data AcQuisition system (TDAQ) room. It has been cleaned, renovated and adapted by reinforcing floors, in-

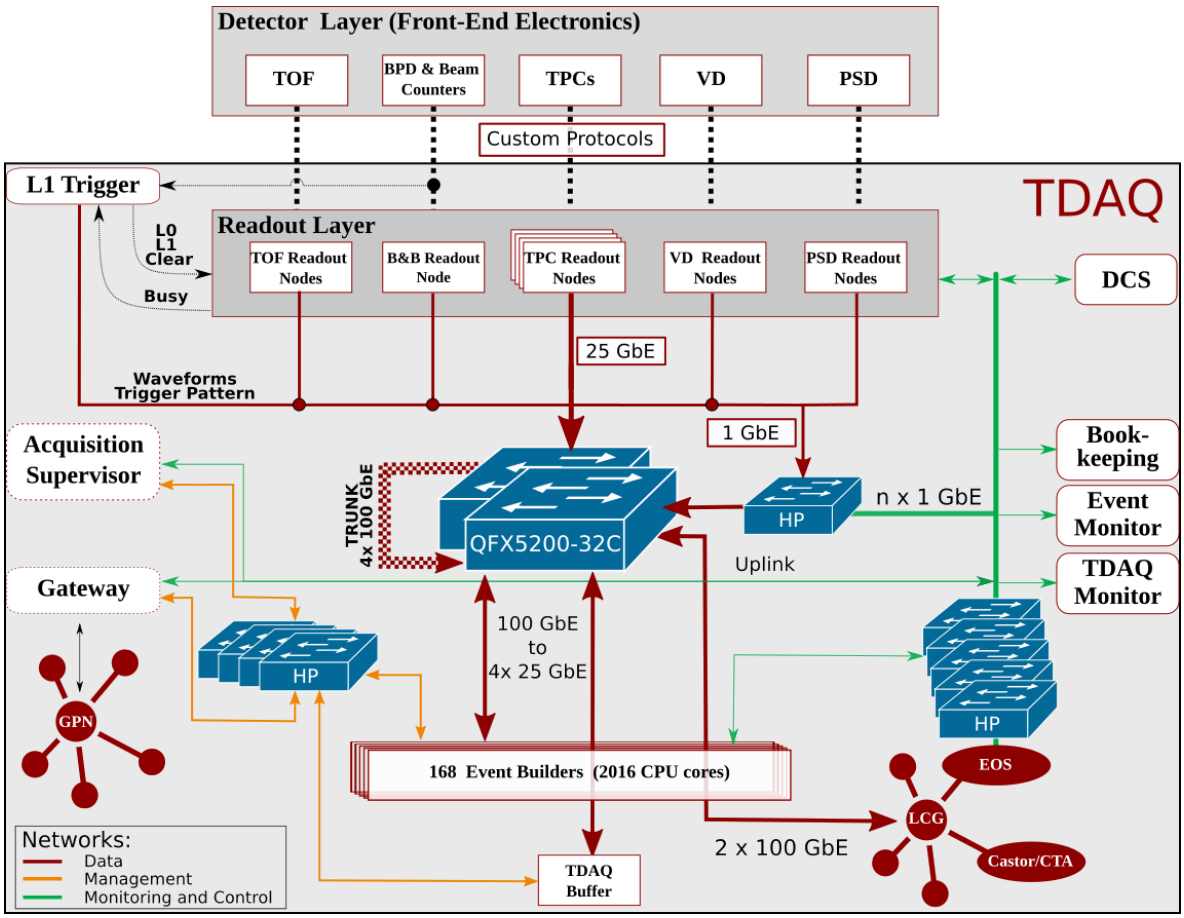

Figure 38: Overview of the new NA61/SHINE trigger and data acquisition system.

stalling a water cooling system and an electricity line. Next, new water-cooled racks were installed, which are capable of cooling all machines needed by the TDAQ online processing software. The TDAQ is in place and infrastructure software has been installed and configured. Tests of the full installation are ongoing and so far generally successful

We are now in the stage of data flow software development and configuration fine-tuning. All crucial components of the data flow software (called pteroDAQtyl) have bee developed and are being tested. In addition, new features are being added such as a web based user interface and additional monitorinc. A schematic of the TDAQ is depicted in Fig. 38.

The Detector Layer is the starting point of data flow. The technologies used to transport data between those layers as well as everything inside the Detector Layer are described in sections dedicated to the corresponding sub-detector.

The Readout Layer consists of nodes, which are sub-event builders. We have already installed nodes for the PSD, BPDs, and all TPCs. Adding nodes for the remaining detectors is planned before end of this year. We already acquired all required hardware. Furthermore, work on the communication library is finished and extensive tests have been done. We plan to perform more testing for the most demanding scenarios.

The Acquisition Supervisor is an integral and central part of the DAQ system and, at the same time, the most crucial one. The hardware has been installed and configured and development of the software is done. Tests of this component are ongoing.

The Event Builders receive sub-events from all nodes and assemble a final event. All Event Builders are in place and and the event building software is operational. It is undergoing tests in order to detect and fix issues related to cooling system, power supply, networking and netbooting. Furthermore, significant progress has been made regarding online processing including development of data reduction methods such as local tracking and machine learning-based noise rejection.

Data storage consists of the TDAQ buffer, EOS, and Castor/CTA. The TDAQ buffer is a disk array capable of storing 700 TB of data. During data taking, as the name suggests, it buffers data before archiving it on Castor/CTA or, in case of test data, on EOS. The data is transferred via two 100 GbE direct optical links to the CERN Computing Center. The links are already operational, but in case of connection loss, the data buffer will hold our data until the connection is restored.

During LS2 the NA61/SHINE trigger system underwent a major upgrade. The old system based on CAMAC components (main logic unit, pattern units, scalers etc.) was replaced by a new system based on modern VME components. The core of the new trigger system is the CAEN V2495 programmable logic unit based on the Altera Cyclone V FPGA. Custom firmware for the CAEN module was developed for this purpose, handling the trigger logic required for efficient operation of the NA61/SHINE detector system. Moreover, the new trigger system incorporates BUSY logic programmed in the FPGA fabric. A custom system allowing distribution of up to three trigger signals to sub-detectors and collection of BUSY signals by means of a standard category-7 S/FTP cable was introduced.

The new (former ALICE) TPC electronics which require a TTC (Timing Trigger Control) signal used by LHC experiments for triggering. For testing, valid TTC trigger sequences were generated in NA61 by a V2495 logic unit coupled with the standard TTCex module. The new TPC electronics were successfully triggered and tested using this setup.

Development of the new trigger system is close to finished: during the 2021 test beam periods devoted to NA61/SHINE the system was tested and successfully commissioned with analog signals from two scintillating beam counters. The custom trigger distribution system was used to send triggers to the BPD and PSD, incorporating DRS4-based readout, and new TPC electronics via the TTC protocol. Online software for configuration, control and monitoring of the trigger was developed and integrated with the pteroDAQtyl framework, providing a uniform software stack across the whole experiment.

The Event Monitor and the DCS have not been yet integrated with the TDAQ system. The work is in progress. The dedicated TDAQ monitoring based on Icinga2 complemented by the Grafana and Prometheus database is partially operational; work is still in progress.

5 Beam periods in 2022 and plans for data taking in 2023-2024

The first NA61/SHINE beam request for 2021-2024 was submitted to the SPSC in 2018 [79]. The Committee subsequently recommended it [80] and the Research Board approved the data taking in 2021 [81]. Due to the COVID-19 pandemic, the schedule of accelerators and the detector upgrade has been modified. In particular, the data taken with the T2K long target and the Pb beams for the open charm programme and nuclear fragmentation cross-section measurements did not occur in 2021. Moreover, in addition to the primary Pb beam, primary oxygen beam is planned for 2023.

The revised data taking schedule presented below takes the above into account and assumes that the data-taking conditions are as in Ref. [79]. Note that the number of collected events is proportional to the duty cycle. Thus it is critical to have it as high as possible.

5.1 Beam periods in 2022

Commissioning and calibration periods:

(i) **April/May 2022**: two weeks of proton beam for the detector commissioning and calibration with hadron beams

(ii) **June/July 2022, during the LEIR commissioning**: one week of Pb beam for the detector commissioning and calibration with heavy-ion beams,

Physics with secondary hadron beams:

(i) **August/September 2022**: 5 weeks of proton beam at 31 GeV/c for data taking for neutrino physics. For detail, see Ref. [82].

Physics with lead beams:

(i) **October/November/December 2022**: 7 weeks of Pb beam at 150A GeV/c for charm hadron measurements in Pb+Pb collision. For detail see Ref. [82],

(ii) **December 2022**: one week of a secondary (fragmented) light-ion beam at 13A GeV/c for nuclear fragmentation cross-section measurements. For detail see Ref. [82],

5.2 Request for measurements in 2023-2024

The measurements requested for 2023-2024 are a continuation of measurements with hadron and lead beams requested for 2022. In addition, we request measurements with oxygen beams in 2023. Note that these requests do not yet include any additional running that may be associated with the low-energy hadron beam discussed in the accompanying letter of intent.

Physics with secondary hadron beams:

(i) **2023**: four weeks of a K+ beam at 60 GeV/c for thin-target graphite cross-section measurements. For detail, see Ref. [82],

(ii) **2023**: two weeks of a proton beam at 120 GeV/c for thin-target titanium cross-section measurements. For detail, see Ref. [82],

(iii) **2024**: four weeks of a 120 GeV/c proton beam for measurements on an LBNF/DUNE prototype target. For detail, see Ref. [82].

Physics with lead beams:

(i) **2023**: six weeks of Pb beam at 150A GeV/c for charm hadron measurements in Pb+Pb collisions

(ii) **2023**: *optional (in case the oxygen beam is not available) two weeks of a secondary light-ion beam at 13A GeV/c for nuclear fragmentation cross-section measurements for cosmic-ray physics*,

(iii) **2024**: six weeks of Pb beam at 40A GeV/c for charm hadron measurements in Pb+Pb collisions.

For detail on the open charm-related beam request, see Sec. 4.4 and, in particular Table 2, of the 2018 Addendum [83]. For details on the secondary light-ion beam request for cosmic-ray physics, see Sec. 7.3 of 2018 Addendum [83].

Physics with oxygen beams:

(i) **2023**: two weeks of oxygen beams at 40A GeV/c and 150A GeV/c for the onset of fireball studies, detail see below,

(ii) **2023**: two weeks of primary and fragmented oxygen beams at 13A GeV/c, 40A GeV/c and 150A GeV/c for nuclear fragmentation cross-section measurements for cosmic-ray physics. For detail, see below.

NA61/SHINE requests the SPSC recommendation of the measurements planned for 2022-2024 as given above.

5.2.1 Justification of measurements with oxygen beam

Oxygen beam for system-size dependence.
Measurements of the system size dependence of hadron production properties at different collision energies were carried out by NA61/SHINE to search for the deconfinement critical point and establish system size dependence of effects related to the onset of deconfinement. The selected hadron production properties change rapidly when increasing the nuclear mass of colliding nuclei between Be and Ar. As a result, an unexpected phenomenon has been discovered: the onset of fireball, for recent review see Ref. [84]. However, this conclusion is in tension with relatively low-statistics results of NA49 obtained with secondary C and Si beams (see Fig. 39). The primary oxygen beam planned in 2023 gives a unique opportunity to resolve the tension with high-statistics measurements.

Oxygen beam for cross-section measurements.
The use of a fragmented oxygen beam could provide a source of light ions for the measurement of fragmentation relevant for the propagation of cosmic rays in the Galaxy. As illustrated in Fig. 40, a beam of fragmented ^{16}O nuclei has properties that are complementary to the one obtained from fragmented ^{207}Pb. Whereas for primary lead, the full range of

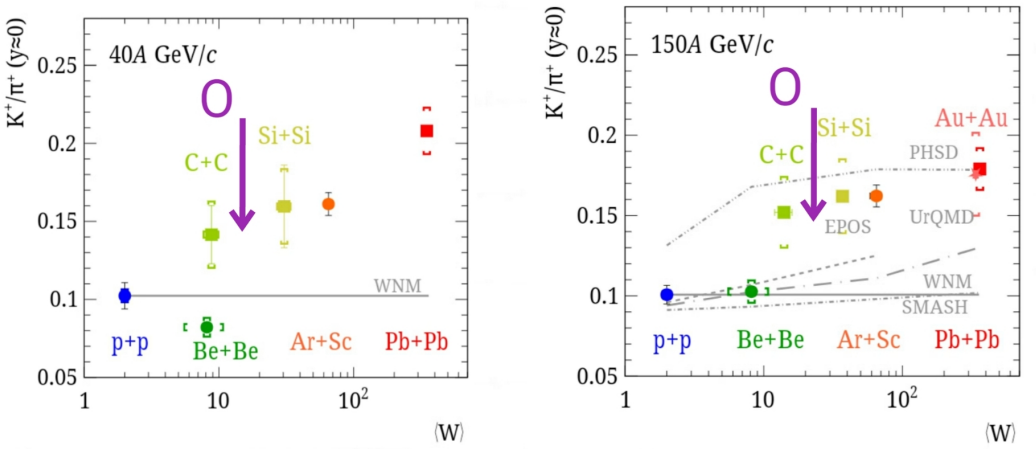

Figure 39: The system-size dependence of the K^+/π^+ particle yields ratio at mid-rapidity at 40A GeV/c (*left*) and 150A GeV/c (*right*) for central ion-ion collisions, as well as inelastic p+p interactions. Both statistical (vertical bars) and systematic (shaded bands) uncertainties are shown. Clearly, data with oxygen beams are needed to resolve the tension between the results.

cosmic-ray related isotopes [2] can be measured simultaneously, fragmented ^{16}O nuclei allow to measure the most important isotopes (^{12}C, ^{14}N, ^{16}O) with an estimated ratio of wanted to all ions close to 20% whereas this ratio is only $\sim$ 2% for primary lead. Other light fragments ($A \leq 16$) are also accessible with dedicated beamline settings, $A/Z \neq 2$. Furthermore, primary oxygen at different energies would allow us to investigate the energy-dependence (or lack thereof) of nuclear fragmentation.

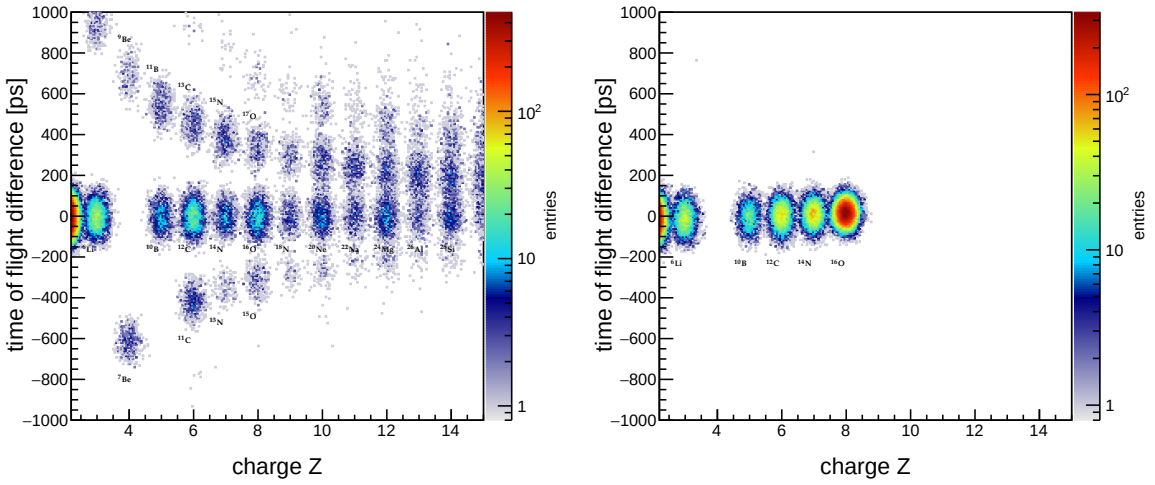

Figure 40: Simulation of the time-of-flight and charge distribution arriving at the NA61/SHINE detector for secondary ions produced by ^{207}Pb (left) and ^{16}O nuclei on a 300 mm Be target at $p_{\text{beam}} = 13$ A GeV/c using FLUKA. Particles were selected within a $\pm$1% rigidity acceptance and at a polar angle of $\leq$ 1 mrad.

[2] These are, in order of importance, ^{16}O, ^{12}C, ^{14}N, ^{10}B, ^{11}B, ^{13}C, ^{15}N, see [83] and [85] for further details.

6 Summary

This NA61/SHINE annual report briefly presents the status and plans of the NA61/SHINE experiment [1] at the CERN SPS. The report refers to the period October 2020 – October 2021.

The summary of this report is as follows:

(i) New physics results, final and preliminary, were released (see Section 2). They include:

Results relevant for the NA61/SHINE study of the onsets of deconfinement and fireball and search for the critical point:

(a) π^- production in central Be+Be collisions at 19A–150A GeV/c

(b) π^- production in central Ar+Sc collisions at 13A–150A GeV/c

(c) multiplicity fluctuations of identified hadrons in inelastic p+p collisions at 31–158 GeV/c

(d) proton intermittency in Ar+Sc at 150A GeV/c
and Pb+Pb at 30A GeV/c

(e) intermittency of negatively charged hadrons in Pb+Pb at 30A GeV/c

(f) rapidity dependence of higher-order moments of multiplicity and net-charge in inelastic p+p collisions at 158 GeV/c

(g) higher-order moments of multiplicity and net-charge in (inelastic p+p and) central Be+Be and Ar+Sc collisions

Further new physics results within the strong interaction program:

(a) two-particle correlations in azimuthal angle and pseudorapidity in central Be+Be collisions at 19A–150A GeV/c

(b) $\Xi(1530)^0$ and $\overline{\Xi}(1530)^0$ production in inelastic p+p collisions at 158 GeV/c

(c) K^0_S production in inelastic p+p collisions at 158 GeV/c

The results obtained within the NA61/SHINE reference measurements for long-baseline neutrino oscillation experiments at J-PARC and Fermilab as well as cosmic-ray experiments (CR) include:

(a) hadron spectra in p+C and p+Al interactions at 60 GeV/c (FNAL)

(b) hadron spectra in p+C interactions at 120 GeV/c (FNAL)

(c) hadron production in NOvA replica target (FNAL)

(d) production cross-section of p+C interactions at 31 GeV/c for T2K (J-PARC)

(e) hadron production in π^-+C interactions (CR)

(f) fragmentation cross-section for Galactic Cosmic Rays (CR)

(g) high statistics π^+, π^-, K^+, K^-, p, $\overline{p}$ spectra in inelastic p+p collisions at 158 GeV/c

(ii) Software and calibration modifications (see Section 3), in particular, include:

(a) development of the Forward-ToF calibration and reconstruction software

(b) development of the Vertex Detector reconstruction software

(c) development of the $\mathrm{d}E\,/\,\mathrm{d}x$ calibration software

(d) development of the magnetic field calibration software

(iii) Detector upgrade status is reported in Section 4. It includes:

(a) Vertex Detector

(b) Time Projection Chambers

(c) Time-of-Flight Detector

(d) Projectile Spectator Detectors

(e) Beam Postion Detectors

(f) Trigger and Data Acquisition Systems

(iv) The requested beam periods in 2022 are presented in Section 5.1:

Commissioning and calibration periods:

(a) **April/May 2022**: two weeks of a proton beam for the detector commissioning and calibration with hadron beams

(b) **June/July 2022, during the LEIR commissioning**: one week of a Pb beam for the detector commissioning and calibration with heavy-ion beams,

Physics with secondary hadron beams:

(a) **August/September 2022**: 5 weeks of proton beam at 31 GeV/c for data taking for neutrino physics, for detail see Ref. [82].

Physics with lead beams:

(a) **October/November/December 2022**: 7 weeks of Pb beam at 150A GeV/c for charm hadron measurements in Pb+Pb collisions, for detail see Ref. [82],

(b) **December 2022**: one week of a secondary (fragmented) light-ion beam at 13A GeV/c for nuclear fragmentation cross-section measurements, for detail see Ref. [82],

(v) Request for measurements in 2023-2024 which the SPSC already recognized as being of the broad physics interest is summarized in Section 5.2. Physics motivation and experimental performance were detailed in 2018 Addendum [79]. The requested measurements are a continuation of the 2022 measurements. The requested beam periods are:

Physics with secondary hadron beams:

(a) **2023**: four weeks of a K+ beam at 60 GeV/c for thin-target graphite cross-section measurements

(b) **2023**: two weeks of a proton beam at 120 GeV/c for thin-target titanium cross-section measurements

(c) **2024**: four weeks of a 120 GeV/c proton beam for measurements on a LBNF/DUNE prototype target.

Physics with lead beams:

(a) **2023**: six weeks of Pb beam at 150A GeV/c for charm hadron measurements in Pb+Pb collisions

(b) **2024**: six weeks of Pb beam at 40A GeV/c for charm hadron measurements in Pb+Pb collisions.

Physics with oxygen beams:

(a) **2023**: two weeks of oxygen beams at 40A GeV/c and 150A GeV/c for onset of fireball studies

(b) **2023**: two weeks of a primary and fragmented oxygen beams at 13A GeV/c, 40A GeV/c and 150A GeV/c for nuclear fragmentation cross-section measurements for cosmic-ray physics.

NA61/SHINE requests the SPSC recommendation of the measurements planned for 2023-2024

Acknowledgments

We would like to thank the CERN EP, BE, HSE and EN Departments for the strong support of NA61/SHINE.

This work was supported by the Hungarian Scientific Research Fund (grant NKFIH 123842/123959), the Polish Ministry of Science and Higher Education (grants 667/N-CERN/2010/0, NN 202 48 4339 and NN 202 23 1837, WUT ID-UB), the National Science Centre Poland(grants 2014/14/E/ST2/00018, 2014/15/B/ST2 / 02537 and 2015/18/M/ST2/00125, 2015/19/N/ST2 /01689, 2016/23/B/ST2/00692, DIR/WK/ 2016/2017/ 10-1, 2017/ 25/N/ ST2/ 02575, 2018/30/A/ST2/00226, 2018/31/G/ST2/03910, 2019/34/H/ST2/00585, 2016/21/D/ST2/01983), the Russian Science Foundation, grant 16-12-10176 and 17-72-20045, the Russian Academy of Science and the Russian Foundation for Basic Research (grants 08-02-00018, 09-02-00664 and 12-02-91503-CERN), the Russian Foundation for Basic Research (RFBR) funding within the research project no. 18-02-40086, the Ministry of Science and Higher Education of the Russian Federation, Project "Fundamental properties of elementary particles and cosmology" No 0723-2020-0041, the European Union's Horizon 2020 research and innovation programme under grant agreement No. 871072, the Ministry of Education, Culture, Sports, Science and Technology, Japan, Grant-in-Aid for Scientific Research (grants 18071005, 19034011, 19740162, 20740160 and 20039012), the German Research Foundation DFG (grants GA 1480/8-1 and project 426579465), the Bulgarian Nuclear Regulatory Agency and the Joint Institute for Nuclear Research, Dubna (bilateral contract No. 4799-1-18/20), Bulgarian National Science Fund (grant DN08/11), Ministry of Education and Science of the Republic of Serbia (grant OI171002), Swiss Nationalfonds Foundation (grant 200020117913/1), ETH Research Grant TH-01 07-3 and the Fermi National Accelerator Laboratory (Fermilab), a U.S. Department of Energy, Office of Science, HEP User Facility managed by Fermi Research Alliance, LLC (FRA), acting under Contract No. DE-AC02-07CH11359 and the IN2P3-CNRS (France).

References

[1] N. Antoniou *et al.*, [NA61/SHINE Collab.], "Study of hadron production in hadron nucleus and nucleus nucleus collisions at the CERN SPS," 2006. CERN-SPSC-2006-034.

[2] M. Gazdzicki, M. Gorenstein, and P. Seyboth *Int.J.Mod.Phys.* **E23** (2014) 1430008, arXiv:1404.3567 [nucl-ex].

[3] A. Aduszkiewicz, [NA61/SHINE Collab.], "Report from the NA61/SHINE experiment at the CERN SPS," Tech. Rep. CERN-SPSC-2017-038. SPSC-SR-221, CERN, Geneva, Oct, 2017. http://cds.cern.ch/record/2287091.

[4] A. Acharya *et al.*, [NA61/SHINE Collab.] *Eur. Phys. J. C* **80** no. 10, (2020) 961, arXiv:2008.06277 [nucl-ex]. [Erratum: Eur.Phys.J.C 81, 144 (2021)].

[5] A. Acharya *et al.*, [NA61/SHINE Collab.] *Eur. Phys. J. C* **81** no. 1, (2021) 73, arXiv:2010.01864 [hep-ex].

[6] A. Aduszkiewicz *et al.*, [NA61/SHINE Collab.] *Eur. Phys. J. C* **77** no. 10, (2017) 671, arXiv:1705.02467 [nucl-ex].

[7] A. Acharya *et al.*, [NA61/SHINE Collab.] *Eur. Phys. J. C* **81** no. 5, (2021) 397, arXiv:2101.08494 [hep-ex].

[8] S. V. Afanasiev *et al.*, [NA49 Collab.] *Phys. Rev. C* **66** (2002) 054902, arXiv:nucl-ex/0205002.

[9] C. Alt *et al.*, [NA49 Collab.] *Phys. Rev. C* **77** (2008) 024903, arXiv:0710.0118 [nucl-ex].

[10] N. Abgrall *et al.*, [NA61/SHINE Collab.] *Eur. Phys. J. C* **74** no. 3, (2014) 2794, arXiv:1310.2417 [hep-ex].

[11] M. Gazdzicki *Acta Phys. Hung. A* **4** (1996) 33–44, arXiv:hep-ph/9606473.

[12] M. I. Gorenstein, M. Gazdzicki, and K. Bugaev *Phys. Lett. B* **567** (2003) 175–178, arXiv:hep-ph/0303041.

[13] R. Stock *Phys. Rept.* **135** (1986) 259–315.

[14] M. Gazdzicki and D. Rohrich *Z.Phys.* **C71** (1996) 55–64, arXiv:hep-ex/9607004 [hep-ex].

[15] M. Gazdzicki and M. I. Gorenstein *Acta Phys.Polon.* **B30** (1999) 2705, arXiv:hep-ph/9803462 [hep-ph].

[16] C. Alt *et al.*, [NA49 Collab.] *Eur. Phys. J. C* **45** (2006) 343–381, arXiv:hep-ex/0510009.

[17] E. E. Zabrodin *et al. Phys. Rev. D* **52** (1995) 1316–1342.

[18] V. V. Ammosov *et al.*, [French-Soviet Collab.] *Nuovo Cim. A* **40** (1977) 237.

[19] A. Aduszkiewicz *et al.*, [NA61/SHINE Collab.] *Eur. Phys. J. C* **80** no. 12, (2020) 1151, arXiv:2006.02153 [nucl-ex].

[20] A. Acharya *et al.*, [NA61/SHINE Collab.] *Eur. Phys. J. C* **81** no. 5, (2021) 384, arXiv:2009.01943 [nucl-ex].

[21] A. Acharya *et al.*, [NA61/SHINE Collab.] arXiv:2105.09144 [nucl-ex].

[22] V. Vovchenko and H. Stoecker *Comput. Phys. Commun.* **244** (2019) 295–310, arXiv:1901.05249 [nucl-th].

[23] A. Aduszkiewicz *et al.*, [NA61/SHINE Collab.] *Phys. Rev. C* **102** no. 1, (2020) 011901, arXiv:1912.10871 [hep-ex].

[24] A. Aduszkiewicz *et al.*, [NA61/SHINE Collab.] *Eur. Phys. J. C* **80** no. 5, (2020) 460, arXiv:2001.05370 [nucl-ex].

[25] A. Aduszkiewicz *et al.*, [NA61/SHINE Collab.] *Eur. Phys. J. C* **80** no. 3, (2020) 199, arXiv:1908.04601 [nucl-ex].

[26] A. Aduszkiewicz *et al.*, [NA61/SHINE Collab.] *Eur. Phys. J. C* **76** no. 4, (2016) 198, arXiv:1510.03720 [hep-ex].

[27] A. Aduszkiewicz *et al.*, [NA61/SHINE Collab.] *Eur. Phys. J. C* **80** no. 9, (2020) 833, arXiv:2006.02062 [nucl-ex].

[28] A. Acharya *et al.*, [NA61/SHINE Collab.] arXiv:2106.07535 [hep-ex].

[29] K. Werner, F.-M. Liu, and T. Pierog *Phys.Rev.* **C74** (2006) 044902.

[30] T. Pierog and K. Werner *Nucl.Phys.Proc.Suppl.* **196** (2009) 102–105, arXiv:0905.1198 [hep-ph].

[31] S. Bass *et al. Prog.Part.Nucl.Phys.* **41** (1998) 255–369, arXiv:nucl-th/9803035 [nucl-th].

[32] M. Bleicher *et al. J.Phys.* **G25** (1999) 1859–1896, arXiv:hep-ph/9909407 [hep-ph].

[33] J. Mohs, S. Ryu, and H. Elfner *J. Phys. G* **47** no. 6, (2020) 065101, arXiv:1909.05586 [nucl-th].

[34] W. Cassing and E. Bratkovskaya *Phys. Rev. C* **78** (2008) 034919, arXiv:0808.0022 [hep-ph].

[35] W. Cassing and E. Bratkovskaya *Nucl. Phys. A* **831** (2009) 215–242, arXiv:0907.5331 [nucl-th].

[36] R. I. Louttit *et al. Phys. Rev.* **123** (1961) 1465–1471.

[37] G. Alexander, O. Benary, G. Czapek, B. Haber, N. Kidron, B. Reuter, A. Shapira, E. Simopoulou, and G. Yekutieli *Phys. Rev.* **154** (1967) 1284–1304.

[38] R. L. Eisner *et al. Nuclear Physics B* **123** (1977) 361–381.

[39] M. Firebaugh *et al. Phys. Rev.* **172** (1968) 1354–1369.

[40] V. Blobel *et al.*, [Bonn-Hamburg-Munich Collab.] *Nucl. Phys. B* **69** (1974) 454–492.

[41] H. Fesefeldt, W. M. Geist, J. Hofmann, U. Idschok, and D. Luers, [Bonn-Hamburg-Munich Collab.] *Nucl. Phys. B* **147** (1979) 317–335.

[42] M. Y. Bogolyubsky *et al. Sov. J. Nucl. Phys.* **50** (1989) 424.

[43] V. V. Ammosov *et al. Nucl. Phys. B* **115** (1976) 269–286.

[44] M. Alston-Garnjost, J. Erwin, J. H. Klems, W. Ko, R. L. Lander, D. E. Pellett, and P. M. Yager *Phys. Rev. Lett.* **35** (1975) 142.

[45] J. Chapman *et al. Phys.Lett.* **B47** (1973) 465–468.

[46] D. Brick *et al. Nucl.Phys.* **B164** (1980) 1.

[47] K. Jaeger *et al. Phys.Rev.* **D11** (1975) 2405.

[48] A. Sheng *et al. Phys. Rev. D* **11** (1975) 1733.

[49] F. LoPinto *et al. Phys.Rev.* **D22** (1980) 573–581.

[50] J. L. Bailly *et al.*, [EHS-RCBC Collab.] *Z. Phys. C* **35** (1987) 309.

[51] R. D. Kass *et al. Phys. Rev. D* **20** (Aug, 1979) 605–614.

[52] H. Kichimi *et al. Phys. Rev. D* **20** (Jul, 1979) 37–52.

[53] A. Bialas and M. Gazdzicki *Phys. Lett. B* **252** (1990) 483–486.

[54] T. Czopowicz, "Search for critical point via intermittency analysis in NA61/SHINE," in *the International conference on Critical Point and Onset of Deconfinement* . 2021. https://indico.cern.ch/event/985460/contributions/4264620/.

[55] H. Adhikary, "Search for the QCD critical point by the NA61/SHINE experiment," in *10th International Conference on New Frontiers in Physics* . 2021. https://indico.cern.ch/event/1025480/contributions/4456978/.

[56] M. Gazdzicki, "NA61/SHINE Experiment Physics Program," in *RHIC Beam Energy Scan and Beyond* . 2021. https://conferences.lbl.gov/event/642/contributions/4775/.

[57] M. Maćkowiak-Pawłowska, "NA61/SHINE results on fluctuations and correlations at CERN SPS energies," in *the International conference on Critical Point and Onset of Deconfinement* . 2021. https://indico.cern.ch/event/985460/contributions/4264609/.

[58] A. Borucka, "Multiplicity and net-charge fluctuations in ion+ion collisions at the SPS energies," in *The 20th Lomonosov Conference on Elementary Particle Physics*. 2021. https://indico.cern.ch/event/969765/.

[59] J. Cybowska, "New results on fluctuations in NA61/SHINE experiment," in *50th International Symposium on Multiparticle Dynamics*. 2021. https://indico.cern.ch/event/848680/contributions/4434216/.

[60] M. Maćkowiak-Pawłowska, [NA61/SHINE Collab.] *Nucl. Phys. A* **1005** (2021) 121753, arXiv:2002.04847 [nucl-ex].

[61] L. Adamczyk *et al.*, [STAR Collab.] *Phys. Rev. Lett.* **113** (2014) 092301, arXiv:1402.1558 [nucl-ex].

[62] A. Acharya *et al.*, [NA61/SHINE Collab.] *Phys. Rev. D* **103** no. 1, (2021) 012006, arXiv:2010.11819 [hep-ex].

[63] A. Carroll *et al. Phys. Lett.* **B80** (1979) 319.

[64] N. Amin, [NA61/SHINE Collab.] *PoS* **ICRC2021** (2021) 102.

[65] A. Aduszkiewicz *et al.*, [NA61/SHINE Collab.], "Feasibility Study for the Measurement of Nuclear Fragmentation Cross Sections with NA61/SHINE at the CERN SPS," 2017. CERN-SPSC-2017-035 ; SPSC-P-330-ADD-9.

[66] M. Unger, [NA61/SHINE Collab.] *PoS* **ICRC2019** (2019) 446, arXiv:1909.07136 [astro-ph.HE].

[67] P. von Doetinchem, K. Perez, T. Aramaki, S. Baker, S. Barwick, R. Bird, M. Boezio, S. Boggs, M. Cui, A. Datta, F. Donato, C. Evoli, L. Fabris, L. Fabbietti, E. F. Bueno, N. Fornengo, H. Fuke, C. Gerrity, D. G. Coral, C. Hailey, D. Hooper, M. Kachelriess, M. Korsmeier, M. Kozai, R. Lea, N. Li, A. Lowell, M. Manghisoni, I. Moskalenko, R. Munini, M. Naskret, T. Nelson, K. Ng, F. Nozzoli, A. Oliva, R. Ong, G. Osteria, T. Pierog, V. Poulin, S. Profumo, T. Pöschl, S. Quinn, V. Re, F. Rogers, J. Ryan, N. Saffold, K. Sakai, P. Salati, S. Schael, L. Serksnyte, A. Shukla, A. Stoessl, J. Tjemsland, E. Vannuccini, M. Vecchi, M. Winkler, D. Wright, M. Xiao, W. Xu, T. Yoshida, G. Zampa, and P. Zuccon *Journal of Cosmology and Astroparticle Physics* **2020** no. 08, (Aug, 2020) 035–035, arXiv:2002.04163 [astro-ph.HE]. https://doi.org/10.1088/1475-7516/2020/08/035.

[68] D.-M. Gomez-Coral, A. Menchaca Rocha, V. Grabski, A. Datta, P. von Doetinchem, and A. Shukla *Physical Review D* **98** no. 2, (2018) 023012, arXiv:1806.09303 [astro-ph.HE].

[69] A. Shukla, A. Datta, P. von Doetinchem, D.-M. Gomez-Coral, and C. Kanitz *Physical Review D* **102** (Sep, 2020) 063004, 2006.12707. http://dx.doi.org/10.1103/PhysRevD.102.063004.

[70] A. Merzlaya, 2021. PhD Thesis, Jagiellonian University Krakow, https://cds.cern.ch/record/2771816.

[71] M. Kapishin, [BM@N Collab.] *Eur. Phys. J. A* **52** no. 8, (2016) 213.

[72] V. Babkin *et al. Nucl. Instrum. Meth.* **A824** (2016) 490–492.

[73] M. G. Buryakov, V. A. Babkin, V. M. Golovatyuk, S. V. Volgin, and M. M. Rumyantsev *Phys. Part. Nucl. Lett.* **13** no. 5, (2016) 532–534.

[74] http://afi.jinr.ru/TDC72VHL.

[75] J. Liu *et al. Nucl. Instrum. Meth. A* **925** (05, 2019) 53–59.

[76] https://www.analog.com/media/en/technical-documentation/data-sheets/ADL5565.pdf.

[77] https://www.analog.com/media/en/technical-documentation/data-sheets/AD8009.pdf.

[78] Hamamamtsu. https://www.hamamatsu.com/eu/en/product/type/S13804/index.html.

[79] A. Aduszkiewicz, [NA61/SHINE Collaboration Collab.], "Reply to the SPSC questions on Addendum CERN-SPSC-2018-008 entitled Study of Hadron-Nucleus and Nucleus-Nucleus Collisions at the CERN SPS: Early Post-LS2 Measurements and Future Plans ," Tech. Rep. CERN-SPSC-2018-019. SPSC-P-330-ADD-11, CERN, Geneva, Jun, 2018. https://cds.cern.ch/record/2621751.

[80] "Minutes of the 130th Meeting of the SPSC, Thursday and Friday, 7-8 June 2018," Tech. Rep. CERN-SPSC-2018-020. SPSC-130, CERN, Geneva, Jun, 2018. http://cds.cern.ch/record/2622174.

[81] "Minutes of the 232nd meeting of the Research Board, held on 11 March 2020," Tech. Rep. CERN-DG-RB-2020-495. M-232, CERN, Geneva, Mar, 2020. http://cds.cern.ch/record/2712812.

[82] L. Fields and P. Podlaski, [NA61/SHINE Collaboration Collab.], "Report from the NA61/SHINE experiment at the CERN SPS," tech. rep., CERN, Geneva, Oct, 2020. https://cds.cern.ch/record/2739340.

[83] A. Aduszkiewicz, [NA61/SHINE Collaboration Collab.], "Study of Hadron-Nucleus and Nucleus-Nucleus Collisions at the CERN SPS: Early Post-LS2 Measurements and Future Plans," Tech. Rep. CERN-SPSC-2018-008. SPSC-P-330-ADD-10, CERN, Geneva, Mar, 2018. https://cds.cern.ch/record/2309890.

[84] M. Gazdzicki and P. Seyboth arXiv:1506.08141 [nucl-ex].

[85] Y. Genolini, D. Maurin, I. Moskalenko, and M. Unger *submitted to PRC* (2018) , arXiv:1803.04686 [astro-ph.HE].